Role of fluid injection on earthquake size in dynamic rupture simulations on rough faults

Jeremy Maurer[1], Eric M Dunham[2], and Paul Segall[2]

[1]Missouri University of Science and Technology
[2]Stanford University

November 21, 2022

Abstract

An outstanding question for induced seismicity is whether the volume of injected fluid and/or the spatial extent of the resulting pore pressure and stress perturbations limit rupture size. We simulate ruptures with and without injection-induced pore pressure perturbations, using 2-D dynamic rupture simulations on rough faults. Ruptures are not necessarily limited by pressure perturbations when 1) background shear stress is above a critical value, or 2) pore pressure is high. Both conditions depend on fault roughness. Stress heterogeneity from fault roughness primarily determines where ruptures stop; pore pressure has a secondary effect. Ruptures may be limited by fluid volume or pressure extent when background stress and fault roughness are low, and the maximum pore pressure perturbation is less than 10% of the background effective normal stress. Future work should combine our methodology with simulation of the loading, injection, and nucleation phases to improve understanding of injection-induced ruptures.

Role of fluid injection on earthquake size in dynamic rupture simulations on rough faults

Jeremy Maurer[1,2], Eric M. Dunham[1], Paul Segall[1]

[1]Deptartment of Geophysics, Stanford University, Stanford, CA
[2]Now at Missouri University of Science and Technology, Rolla, MO

Key Points:

- Rupture size is not necessarily limited by the volume of injected fluid in earthquake simulations with imposed pore pressure perturbations
- Stress heterogeneity arising from geometric roughness may be the primary cause for rupture termination on rough faults
- High initial shear stress or pore pressure can trigger a rupture larger than the volume-based magnitude limit on faults with low roughness

Corresponding author: J. Maurer, `jmaurer@mst.edu`

Abstract

An outstanding question for induced seismicity is whether the volume of injected fluid and/or the spatial extent of the resulting pore pressure and stress perturbations limit rupture size. We simulate ruptures with and without injection-induced pore pressure perturbations, using 2-D dynamic rupture simulations on rough faults. Ruptures are not necessarily limited by pressure perturbations when 1) background shear stress is above a critical value, or 2) pore pressure is high. Both conditions depend on fault roughness. Stress heterogeneity from fault roughness primarily determines where ruptures stop; pore pressure has a secondary effect. Ruptures may be limited by fluid volume or pressure extent when background stress and fault roughness are low, and the maximum pore pressure perturbation is less than 10% of the background effective normal stress. Future work should combine our methodology with simulation of the loading, injection, and nucleation phases to improve understanding of injection-induced ruptures.

Plain Language Summary

Earthquakes can be induced or triggered by fluid injected deep underground, if the fluid encounters faults. Previous studies of induced seismicity at different injection sites around the world have empirically found that in many cases the maximum magnitude earthquake may be predicted from the total volume of injected fluid. However, this is not always the case, and the level and heterogeneity of pre-existing stress on faults likely plays an important role in determining the final earthquake size. In this paper, we use numerical simulations of earthquakes to quantify one source of stress heterogeneity - that arising from geometric roughness - and study how changes in pore pressure and stress from fluid injection interact with pre-existing stress to influence earthquake size. We find that earthquakes are not limited by the injected volume, except under specific conditions. Instead, earthquakes stop where pre-existing conditions are unfavorable for continued rupture; in our case because of bends in the fault geometry. Earthquakes can well exceed the predicted maximum magnitude, depending on the pre-existing stress on the fault, how rough it is, and the magnitude and extent of the perturbation from injection.

1 Introduction

An important question in the study of induced seismicity is whether earthquake magnitudes are limited by the volume of injected fluid or some other injection-related parameter [e.g., *Baisch et al.*, 2010; *Shapiro et al.*, 2011, 2013; *McGarr*, 2014; *McGarr and Barbour*, 2017; *Maurer and Segall*, 2018], or follow naturally-occurring (Gutenberg-Richter) size variability [*van der Elst et al.*, 2016]. For example, *McGarr and Barbour* [2017] propose an upper bound on seismic moment released by induced earthquakes, $M_0^{\max}$, defined by

$$M_0^{\max} = 2G\Delta V \tag{1}$$

where G is shear modulus, and ΔV is injected volume. The premise of such an approach is that pore pressure diffuses through the medium, perturbing the effective stress in a finite volume of crust sufficient to induce and maintain rupture, while stress conditions outside the perturbed region do not allow rupture. To evaluate this hypothesis, we consider the behavior of individual simulated ruptures perturbed by spatially-variable pore pressure increases.

Linear elastic fracture mechanics predicts that under uniform background stress conditions and constant fracture energy, a crack introduced to an elastic solid will grow unstably if its length exceeds a critical value a_c. Assuming linear slip-weakening friction on a pre-existing fault, a_c is proportional to the ratio of peak minus residual strength $(\tau^p - \tau^r)$ and the square of the static stress drop $\Delta\tau$ [*Andrews*, 1976]:

$$a_c = \frac{(\tau^p - \tau^r)G}{(\Delta\tau)^2}\frac{f}{(1-\nu)}d_c \tag{2}$$

where G is shear modulus, ν is Poisson's ratio, d_c is the slip-weakening distance, and f is a factor related to the geometry of the problem. In this scenario, there are two possibilities: a crack that does not reach half-length a_c will naturally self-arrest, while a crack that does will slip indefinitely. *Galis et al.* [2017] applied this reasoning to fluid-induced earthquakes to estimate the size of the largest self-arresting ruptures for spatially-variable peak strength. They considered a stress perturbation due to pore pressure in an otherwise-uniform background stress, approximated as a point load. Since background stress is uniform, when the stress is low the localized strength drop provided by pore pressure drives slip into the (unfavorable) stress environment beyond the pressurized zone. If the background shear stress is high enough, the rupture will continue to grow without limit.

Norbeck and Horne [2018] considered quasi-dynamic simulations of induced earthquakes on flat faults with linear slip weakening friction. Based on their simulations, they proposed that induced earthquakes are governed by the ratio $\tau^b/f^D\bar{\sigma}_0 = f^b/f^D$. ($f^b$ is the initial background shear to effective normal stress ratio, f^D is dynamic friction, and

$\bar{\sigma}_0 = \sigma_0 - \Delta p$, where σ_0 is the total normal stress and Δp is the pore pressure.) Events on faults for which $f^b/f^D < 1$ were limited to the pressurized zone, while $f^b/f^D > 1$ resulted in runaway ruptures, irrespective of volume injected.

In these studies, the only source of stress heterogeneity is that of the perturbations in pore pressure. However, pre-existing stress heterogeneity on faults occurs due to geometric roughness and past fault slip, among other sources. *Dempsey and Suckale* [2016] and *Dempsey et al.* [2016] investigated the role of heterogeneity on the size distribution of induced earthquakes on 1-D flat faults using a fracture mechanics approach. They solved the crack equation of motion numerically [*Freund*, 1998] for a suite of stochastic (fractal) shear stress profiles. Ruptures arrest naturally due to variations in shear stress, and *Dempsey and Suckale* [2016] showed that the distribution of rupture size was controlled by the interaction between the spatial distribution of pore pressure and the statistical characteristics of the fractal stress profiles. In their model, stress heterogeneity was imposed as an initial condition, and the rupture size calculation did not account for the potential effects of fault roughness (which influences both shear and normal tractions) and off-fault plasticity. These effects result in fracture energy that cannot be predicted *a priori*, and higher background stress required for rupture [*Dieterich and Smith*, 2009; *Fang and Dunham*, 2013].

In this study, we address these issues and explore the hypothesis that induced earthquakes are limited in size by the magnitude and/or spatial extent of the pore pressure perturbation, in the context of 1-D rough (fractal) faults embedded in a 2-D elasto-visco-plastic medium and obeying a rate-state friction law with strong dynamic weakening [*Dunham et al.*, 2011a,b]. In contrast to the slip-weakening models discussed above, rate-state friction does not have a well-defined residual strength. However, for strong rate weakening friction there exists a critical stress level τ^{pulse}, at which self-sustaining rupture on flat faults is just possible [*Zheng and Rice*, 1998; *Dunham et al.*, 2011a]. When the background shear stress is close to τ^{pulse} (referred to here as "low-stress"), ruptures are pulse-like: slip occurs in a narrow pulse just behind the rupture front, and shear strength recovers behind the rupture tip [e.g., *Cochard and Madariaga*, 1994; *Beeler and Tullis*, 1996; *Zheng and Rice*, 1998].

We simulate earthquakes with and without pore pressure and stress perturbations to determine whether rupture size is limited by the volume of injected fluid and/or the spatial extent of the stress changes. Since faults are geometrically rough, we generate several thousand stochastic realizations in order to characterize results statistically. At low background shear stress, one might expect the extent of the stress and pore pressure perturbations to exert some control on rupture lengths. However, we find that events may be larger than the pressurized region even at low stress if the magnitude of the perturbation is sufficiently large. Ruptures are not confined when stress is high, consistent with *Norbeck and Horne* [2018] and *Galis et al.* [2017]. Our results suggest that dynamic effects and *in situ* stress conditions interact with pore pressure and poroelastic stress perturbations to influence rupture size, and that low stress conditions may not be sufficient to guarantee ruptures smaller than an injection-related threshold.

2 Modeling

2.1 2-D dynamic earthquake simulations

We use the 2-D plane strain rupture dynamics code FDMAP [*Kozdon et al.*, 2012, 2013; *Dunham et al.*, 2011a,b] (see Data and Resources). The model employs a rate-and-state friction formulation in the slip law form with strong rate weakening on the fault and Drucker-Prager visco-plasticity in the off-fault material [*Rice*, 1983; *Noda et al.*, 2009; *Dunham et al.*, 2011a]. There is no quasi-static nucleation phase; events are artificially initiated by adding a Gaussian shear stress perturbation at the first time step. Once initiated, the rupture process is entirely self-governed. Faults are 1-D self-similar fractal profiles, and are oriented such that they lie along the $y = 0$ line of the model domain; flat faults are on the line exactly while rough faults follow it on average. Roughness, parameterized by amplitude to wavelength ratio α (Supp Fig. 1), is band-limited, with minimum and maximum wavelengths of 300 m and 60 km. Values of α on natural faults are thought to vary over an order of magnitude or more, ranging from 0.001 or less on mature faults like the San Andreas, up to perhaps 0.01 [e.g., *Candela et al.*, 2009, 2012; *Sagy and Brodsky*, 2009; *Brodsky et al.*, 2016; *Fang and Dunham*, 2013]. The initial stress is spatially uniform in the medium; pore pressure can be spatially variable as described in Section 2.3. Resolved tractions on rough faults varies along the fault (See Section 2.2), so prior to simulation, the fault profile is shifted such that the least stable part of the fault is located at the origin, where the initiating stress perturbation is applied.

2.2 Stress and slip on geometrically-rough faults

Fault roughness provides additional resistance to slip above that of friction, hence rougher faults require higher stress levels for events to propagate [*Dieterich and Smith*, 2009; *Fang and Dunham*, 2013]. This effect is termed "roughness drag" by *Fang and Dunham* [2013], and is proportional to slip (s), roughness level (α), and inversely proportional to the minimum roughness wavelength, λ_{min}. In most of our simulations, $\lambda_{\text{min}} = 300$ m and τ^{drag} is approximately 10 MPa $(s/\lambda_{\text{min}})\ (\alpha/10^{-3})^2$; however, τ^{drag} increases as λ_{min} decreases (see Supplemental Material). In comparison with the flat-fault simulations (Figure 1), ruptures on rough faults arrest over a wider range of initial background stress ratios, and may even arrest and then re-nucleate due to interacting stresses around fault bends [*Bruhat et al.*, 2016].

2.3 Pore Pressure Models

FDMAP does not model the nucleation phase of rupture; therefore, we run experiments imposing several different pore pressure distributions as part of the initial conditions. We simulate pore pressure and poroelastic stress changes based on an injector location centered with respect to the fault but offset by 2 km. Events are initiated at the origin, where both the resolved stress ratio (see Section 2.1) and the pore pressure are highest. Figure 1a-c and Supp. Fig. 2 shows pressure and poroelastic stress changes along the $y = 0$ line of the model domain for each pore pressure model.

1. Pressure Model 0 (PM0) is the reference case with no pore pressure perturbation.
2. Pressure Models 1 and 2 (PM1 and PM2; Fig. 1a and b respectively) are two realizations of injection into an infinite 2-D (plane strain) poroelastic medium with uniform poroelastic and hydraulic properties, using line source solutions from *Rudnicki* [1986]. We account for the change in total stress from both poroelasticity and pore-pressure in the medium and on the fault. Pressure decays with distance from the origin r as $\exp(-r^2/4ct)$, with diffusivity c and time t. (Parameters for the simulations are given in Supp. tables 1-2.) The pore pressure profiles used in our simulations are for 1000 days of injection with different rates and diffusivities. Peak pore pressure on the $y = 0$ plane (max Δp) is 2 MPa for PM1 and 19 MPa for PM2, and drops to 10 kPa at 19 km from the origin for PM1 and 12.5 km for PM2 (Figure 1(a-b).

3. In Pressure Model 3 (PM3; Fig. 1c), we introduce a high-permeability (k) zone 20 km wide, oriented perpendicular to the fault in the out-of-plane direction and centered at the origin (initiation region), between two symmetric outer regions with low permeability (Supp. Figs. 3-4). We simulate the same volume of injection as in PM1, the only difference being the presence of the high permeability zone. The resulting pressure distribution drops sharply at the boundaries by $\sim$ 4 MPa on the y= 0 line, introducing an additional length scale into the problem. We solve numerically for the pressure distribution [*Elsworth and Suckale*, 2016] (details in the Supplemental material) and use the pressure to calculate the effective stress in the medium, and ignore poroelastic stress perturbations.

3 Results

3.1 Flat faults with Strong Rate-weakening friction

As a reference, we ran a suite of simulations on flat faults. We show results for PM0, PM2, and PM3 in Figure 1a; note that PM1 ruptures behave qualitatively similar to PM3 but with a smaller effect, so are omitted for clarity. For these simulations, $\bar{\sigma}_0 = 62$ MPa. The stress perturbation required to initiate events results in an slip peak at the origin (see Fig. 1e,f). Ruptures may arrest immediately or transition to a pulse-like or crack-like rupture mode, depending on the stress ratio f^b (Fig. 1d).

For PM0 events (solid circles in Fig. 1a), there is a narrow transition near τ^{pulse} from self-arresting ruptures to full-fault ruptures, over a range less than 3% of $\tau^b/\bar{\sigma}_0$. At low background shear stress ($\lesssim 0.32\bar{\sigma}_0$) and no pore pressure perturbation, ruptures arrest, while at higher stress ruptures are self-sustaining, consistent with previous work [*Zheng and Rice*, 1998; *Dunham et al.*, 2011a; *Gabriel et al.*, 2012].

PM2 ruptures initiate, grow, and become full fault at lower levels and over a broader range of background stress ratios than PM0 simulations, due to the decreased strength from pore pressure in the nucleation region. Ruptures become self-sustaining at $\tau^b/\bar{\sigma}_0 \approx$ 0.30, lower than the reference case, even though the stress beyond ±10 km from the origin ($L_{\text{rup}}/L = 0.33$) is very similar to the unperturbed model. That is, the decrease in pore pressure towards the boundaries results in an increase in fault strength, such that away from the origin the fault is nearly as strong as the unperturbed case. Rupture are able to propagate through the strong region (once initiated inside the weaker perturbed zone), at

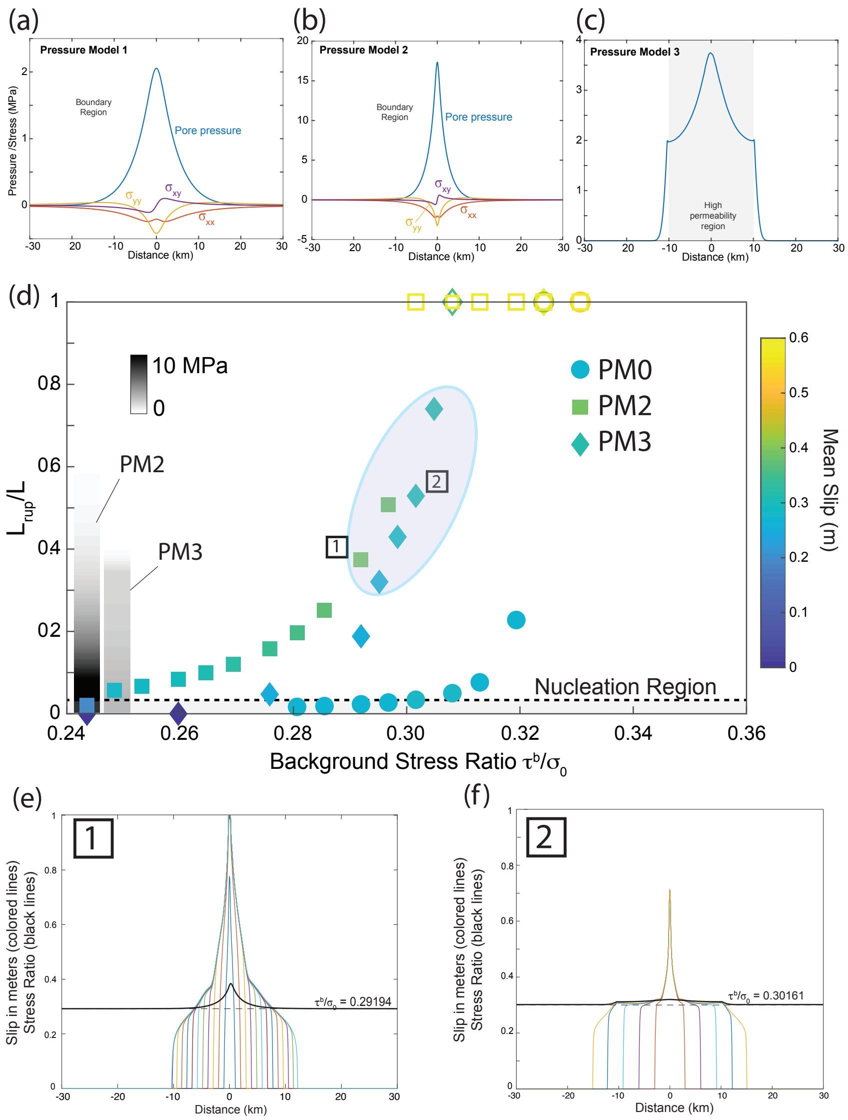

Figure 1. Dynamic ruptures on flat faults. **(a-c)** Pore pressure and poroelastic perturbation along the $y = 0$ line for (a) Pressure Model 1 (PM1), (b) Pressure Model 2 (PM2), and (c) Pore pressure perturbation only for Pressure Model 3 (PM3). The shaded region is the high-k zone. **(d)** Rupture length normalized by fault length (60 km) versus background stress ratio $f^b = \tau^b/\bar{\sigma}_0$ for PM0, PM2, and PM3. Open symbols are for full fault ruptures. The gray-scale colorbars on the left show how pore pressure decays with distance (saturated at 10 MPa for clarity). The colored oval highlights events that are possibly limited by the spatial extent of the pressure perturbation. **(e-f)** Example ruptures corresponding to numbered boxes in (d). Dashed line is background stress level and perturbed initial effective stress ratio is the solid line. Colored lines show cumulative slip at 0.7 second-intervals.

stress levels where they could not initiate. This is due partially to the larger shear stress drop in the nucleation region for the perturbed case, and partially to the strong dynamic weakening. Ruptures at lower stress may arrest due to the increase in fault strength encountered outside the perturbed region (Fig. 1e), consistent with Eq. 1.

PM3 ruptures (solid diamonds in Fig. 1a) show evidence of arresting due to spatially-variable pore pressure. Fig. 1f shows an example, where the rupture begins to propagate at a constant rate, then dies out upon reaching the edge of the perturbed zone. This is the clearest example of pressure controlling where the rupture stops. At higher background stresses, ruptures grow beyond the pressurized zone to the edge of the computational domain. Thus, for PM3 the increase in frictional strength at the edge of the pressurized region may influence rupture arrest for a small range of stress ratios $\sim 0.27 - 0.30$.

To summarize, flat fault simulations show that 1) pore pressure perturbations leads to rupture at lower shear stress (or larger ruptures) relative to the reference case, and 2) the spatial extent of pore pressure perturbations may limit ruptures in a narrow range of stress conditions, but 3) at high shear stress ($\tau^b/\bar{\sigma}_0 > \tau^{\text{pulse}}$) ruptures are unbounded, consistent with the results of *Galis et al.* [2017]. The question we consider next is how geometric roughness impacts rupture size.

3.2 Results on rough faults

Results for rough faults at a background effective normal stress of 62 MPa are shown here; results for 126 MPa are shown in the Supplemental Material. For these simulations, $\alpha = 0.004 - 0.012$ and $f^b \sim 0.015 - 0.45$. Note that the values of f^b are lower than inferred in previous studies of induced seismicity (0.6-0.8; e.g. *Walsh and Zoback* [2016]), which is because the minimum roughness wavelength in the simulations is much larger than that expected on natural faults (see Supplemental Material). Fault strength at high slip speed depends on fault roughness (due to τ^{drag}), thus faults with smaller minimum roughness wavelength require higher stress to rupture (see the Supplemental material for more details).

Figure 2 shows two example simulations on the same fault with identical parameters, one with no pressure perturbation (PM0) and one with perturbed pressure model PM3. Slip in Fig. 2a, without a perturbation, does not extend outside the nucleation region, and therefore is considered an ‘arrested’ rupture, while the simulation with PM3 in Fig. 2b ruptures ∼ 40% of the fault. In this simulation, stress perturbations due to fault geometry dominate the initial stress heterogeneity on the fault (10x larger than the pore pressure perturbation). However, the perturbed rupture propagated outside the nucleation region, suggesting that the length scale over which the pressure perturbation acts is an important factor in determining final rupture size. Comparing the initial and final stresses in Figure 2c and d shows that the PM3 rupture arrests due to encountering low-stress barriers at restraining bends. Supp. Figs. S5 and S6 show additional simulation examples.

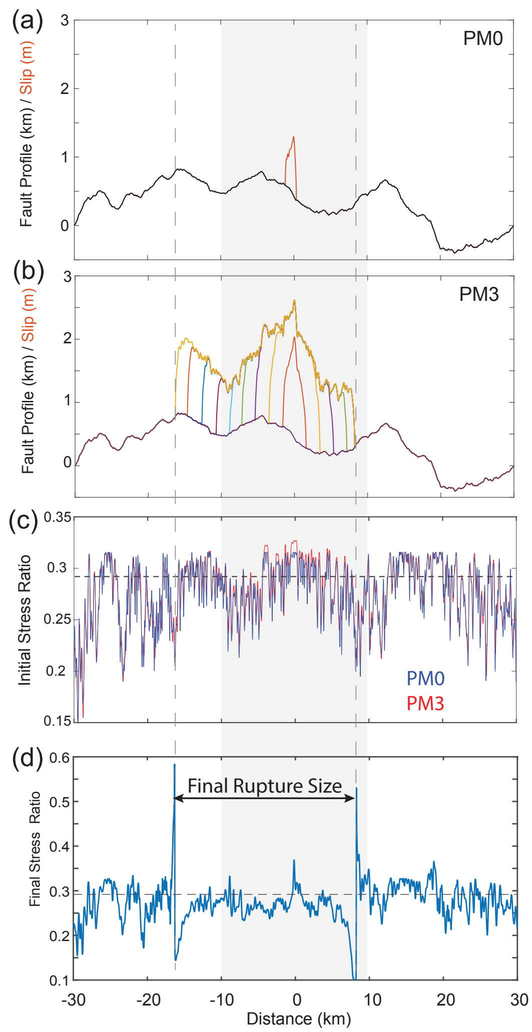

Figure 2. **(a)** Unperturbed (PM0) and **(b)** perturbed (PM3) ruptures for the same fault and background stress ratio ($\bar{\sigma}_0 = 126$ MPa, $f^b = 0.282, \alpha = 0.006$). The shaded area is the high permeability zone and the vertical dashed lines give the termination of the PM3 rupture. **(c)** Initial stress for both simulations; blue=PM0, red=PM3. Horizontal line is the background stress ratio($f^b = \tau^b/\sigma_0$). **(d)** Final stress ratio for PM3 rupture. Horizontal dashed line is $\tau^{\text{pulse}}/\sigma_0$.

In Figure 3 we show summary results for several hundred simulations, illustrating two background stress ratios and roughness levels. The left column in Fig. 3 shows empirical frequency-length distributions, while the right column shows frequency-moment distributions. The gray-scale bars at the top left show the spatial extents of pore-pressure perturbation for the different models. Additional event size distributions are shown in Supp. Figs. S7-S10. Figure 3 demonstrates the importance of the length scale of the pressure perturbation. Pressure models PM1 and PM3 have the same total injected volume, but PM3 ruptures propagate farther than PM1. Pore pressure has less of an impact on rupture size at high roughness.

The right column of Fig. 3 shows frequency-moment distributions. Moment per unit length in the out-of-plane direction (D), is defined as the product of the shear modulus G with the length-averaged slip $s(\xi)$, where ξ is arclength along the fault trace of length L:

$$\frac{M}{D} = G \int_L s(\xi) d\xi \qquad (3)$$

There is a minimum moment imposed by the initiation process of approximately 2×10^{13} N m /m, while the upper bound on moment corresponds to a full fault rupture (60 km) times a few meters of slip, giving a "full-fault" moment between $\sim 10^{15} - 10^{16}$ N m /m, depending on the amount of slip. The injected volume (see Supp. Tables 3-5 for relevant parameters) is $\Delta V = 4 \times 10^3$ m^3/m for PM1 and PM3, and 2×10^4 m^3/m for PM2. $M_0^{\max}$ from Eq. 1 is then 2.8×10^{14} N m/m for PM1 and PM3, and 1.55×10^{15} N m /m for PM2.

At high background stress ($f^b = 0.347$) all of the moment distributions exceed the hypothesized bounds. At low background stress ratios ($f^b = 0.282$) the distributions tend to tail off well before reaching the hypothesized bounds. At best, PM3 ruptures at low stress ($f^b = 0.282$) arrest close to the magnitude limit theorized by *McGarr and Barbour* [2017], which may indicate that pore pressure may have a secondary role in stopping ruptures when roughness and stress are low (and compare to Figure 1f for PM3 rupture on a flat fault). Even at low background stress, the strong pore pressure perturbations (max $\Delta p \sim 30\%$ of the background normal stress) of PM2 are sufficient to induce large ruptures greater than the *McGarr and Barbour* [2017] limit in our simulations (Figure 3, top panel).

Figure 4 and Supp. Figure 11 show perturbed vs. non-perturbed moment for several roughness/stress combinations. As with Figure 3, at higher roughness (Fig. 4c,d), the maximum size of perturbed events is controlled primarily by roughness and background stress,

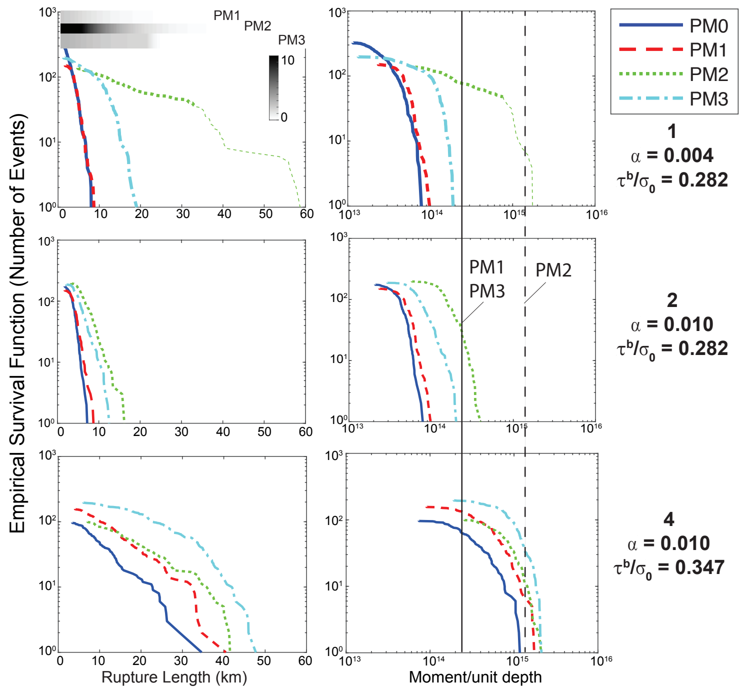

Figure 3. Frequency-length distributions (first column) and frequency-moment distributions (second column) for two roughness and and background stress levels. The y-axis is one minus the cumulative distribution function, times the number of non-failed ruptures. Low roughness/high stress results are not shown; all events are full-fault ruptures. The gray-scale bars at the top of the left column show the spatial extent of the pore pressure perturbation, saturated at 10 MPa. Vertical solid line in the right column represents $M_0^{\max} = 2.8 \times 10^{14}$ N m/m for PM1/PM3, and dashed is 1.55×10^{15} N m /m (PM2). The thinner dashed line segment in the top two panels are simulations that reach one or both ends of the fault.

and secondarily by the injection-induced stress perturbation. In particular, for high stress and high roughness, the largest perturbed event (i.e., out of the whole population of events with the same stress conditions and fault roughness) is less than four times larger than the largest non-perturbed event out of the whole population The perturbation has a stronger impact on rupture size at low roughness. At low stress and roughness (Fig. 4a), strongly-perturbed events (PM2) tend to be much larger (by more than an order of magnitude in moment) than non-perturbed events, while moderate pressure changes (PM1) result in little difference between perturbed and non-perturbed ruptures.

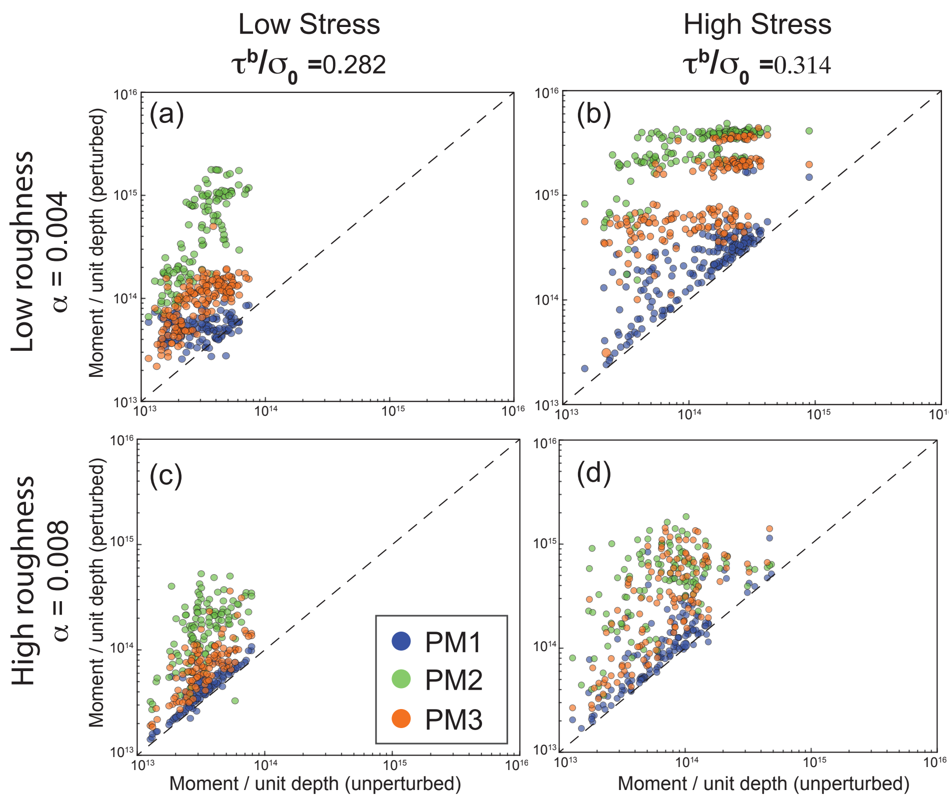

Figure 4. Perturbed versus non-perturbed moment per unit out-of-plane distance for identical fault geometries and background stress. Columns are the same background stress, rows are the same roughness. The two lines of clustered events in the upper-right plot are ruptures that reach one or both ends of the fault and thus do not naturally arrest.

4 Discussion

On flat faults, we find empirically (Fig. 1) that the criteria for when ruptures exceed the pressurized zone is related to the ratio of the background shear stress and τ^{pulse}:

$$\begin{aligned} f^b = \tau^b/\bar{\sigma}_0 > & \tau^{\text{pulse}}/\bar{\sigma}_0 \approx 0.3 \\ & \to \frac{f^b}{(\tau^{\text{pulse}}/\bar{\sigma}_0)} \leq 1 \end{aligned} \tag{4}$$

where the bar in $\bar{\sigma}_0$ emphasizes that this is the effective normal stress. *Zheng and Rice* [1998] showed that faults for which $f^b \approx \tau^{\text{pulse}}/\bar{\sigma}_0$ could sustain pulse-like ruptures, while *Norbeck and Horne* [2018] showed that if this criteria is met only locally inside of a pressurized zone, ruptures would be limited by the spatial extent of the zone. Replacing f^D in their slip-weakening simulations with $\tau^{\text{pulse}}/\bar{\sigma}_0$ as a modified criteria, our results qualitatively agree with this conclusion.

In contrast to flat faults, on rough faults (with the parameter ranges we have considered: $10^{-3} < \alpha < 10^{-2}$, $\bar{\sigma}_0 \sim 100$ MPa, $\Delta p \sim 1 - 10$ MPa), pore pressure plays a less important role compared to stress perturbations from geometry. Comparison of rupture magnitudes with those predicted by the *McGarr and Barbour* [2017] relationship indicates that ruptures are not limited by the volume injected; either ruptures arrest due to local high-strength patches, or ruptures exceed the hypothesized boundary. The exception is at low roughness and low background stress, where pore pressure decay may result in ruptures arresting in some cases (Figure 3, low stress PM3 ruptures; cf. Figure 1f). These results suggest that the role of pore pressure in limiting rupture size is secondary to that of the *in situ* stress level and heterogeneity.

The results shown in Figure 3 demonstrate that stress heterogeneity arising from fault roughness exerts primary control on stopping ruptures. However, the spatial distribution of pore pressure clearly plays an important role. Comparing PM1 with PM3 ruptures, which have identical injected volume, PM3 ruptures can reach larger size than PM1 ruptures regardless of stress and roughness, and can be larger than PM2 ruptures at high roughness. This may be because the higher available stress drop from the perturbation distributed over a smaller region is not able to overcome the resistance to slip of very poorly oriented fault segments. Thus, the pore pressure perturbations does impact rupture size, but not in the simple manner suggested by Equation 1. Instead, the pre-existing stress state, including both the mean value and the heterogeneity in stress and interactions with the spatial distribution and magnitude of the pore pressure perturbation to impact rupture size.

The results presented in this study demonstrate that the addition of pore pressure to a given background stress state encourages larger ruptures. However, the results do not address whether the pore pressure distributions considered in this study are realistic in natural settings. For example, perhaps events in Figure 3 exceeding the moment limits of Eq. 1 would have nucleated a smaller event at a lower pore pressure. While it is possible to reach high pore pressure consistent with PM2 in localized areas around an injector [*Häring et al.*, 2008], this level of pore pressure would not be expected at large depths and/or distances from the injector. Thus, care must be taken in interpreting the results. However, no events at low stress exceed the hypothesized limits without additional pore pressure, so the artificial initiation alone is not sufficient to produce large events.

Future research should address the limitations of this study and focus on sequence simulations of induced earthquakes that account for nucleation and aseismic slip processes explicitly, and allow rupture to occur naturally, rather than artificially imposing a particular pressure perturbation and comparing rupture size. Simulations that account for both gradual pressure build-up as well as the dynamic effects that occur during rupture are required to fully resolve how stress and frictional strength change throughout the earthquake cycle, and determine whether the results presented here are relevant in more realistic scenarios.

5 Conclusions

We have conducted an extensive set of simulations to explore how injection-induced pore pressure and poroelastic stress changes impact the size of dynamic ruptures on rough faults. We find that rupture size is not limited by injected volume except when roughness, background stress, and the pressure perturbation are all low. Events can grow beyond the pressurized zone and exceed published magnitude limits if $\tau^b > \tau^{\text{pulse}}$ or the pore pressure perturbation is large. Higher pore pressure tends to result in larger ruptures; however, at low background stress and high roughness events never grow as large as published limits. Only in the limited case of low to no roughness and low background stress ($\tau^b \leq \tau^{\text{pulse}}$) do events appear to ever be limited in size by the size of the perturbed region. Instead, the results indicate that rupture size is primarily controlled by the *in situ* stress level and heterogeneity, and only secondarily by pressure. This is likely partly due to the stress ratio on geometrically-rough faults varying up to 30-70% from the background level for the parameter ranges considered here, compared to 15% or less for the modeled pressure-induced perturbations. Future research is required to determine whether our results hold for naturally-nucleated earthquakes, but at present we suggest that, once nucleated by fluid injection, induced earthquakes are not required to stop at the boundaries of the pressurized region.

6 Data and Resources

The code for FDMAP is available from https://bitbucket.org/ericmdunham/fdmap. Data from the simulations is available from *Maurer* [2020], last accessed April 13, 2020.

Acknowledgments

This work was funded by the Stanford Center for Induced and Triggered Seismicity at Stanford University. Simulations in this work were carried out using the computing facilities of the Center for Computational Earth and Environmental Science at Stanford University.

References

Andrews, D. J. (1976), Rupture velocity of plane strain shear cracks, *Journal of Geophysical Research*, *81*(32), 5679–5687, doi:10.1029/JB081i032p05679.

Baisch, S., R. Vörös, E. Rothert, H. Stang, R. Jung, and R. Schellschmidt (2010), A numerical model for fluid injection induced seismicity at Soultz-sous-Forêts, *International Journal of Rock Mechanics and Mining Sciences*, *47*(3), 405–413, doi: http://dx.doi.org/10.1016/j.ijrmms.2009.10.001.

Beeler, N. M., and T. E. Tullis (1996), Self-healing slip pulses in dynamic rupture models due to velocity-dependent strength, *Bulletin of the Seismological Society of America*, *86*(4), 1130–1148.

Brodsky, E. E., J. D. Kirkpatrick, and T. Candela (2016), Constraints from fault roughness on the scale-dependent strength of rocks, *Geology*, doi:10.1130/G37206.1.

Bruhat, L., Z. Fang, and E. M. Dunham (2016), Rupture complexity and the supershear transition on rough faults, *Journal of Geophysical Research B: Solid Earth*, *121*(1), 210–224, doi:10.1002/2015JB012512.

Candela, T., F. Renard, M. Bouchon, A. Brouste, D. Marsan, J. Schmittbuhl, and C. Voisin (2009), Characterization of fault roughness at various scales: Implications of three-dimensional high resolution topography measurements, *Pure and Applied Geophysics*, *166*(10-11), 1817–1851, doi:10.1007/s00024-009-0521-2.

Candela, T., F. Renard, Y. Klinger, K. Mair, J. Schmittbuhl, and E. E. Brodsky (2012), Roughness of fault surfaces over nine decades of length scales, *Journal of Geophysical Research: Solid Earth*, *117*(B8), doi:10.1029/2011JB009041.

Cochard, A., and R. Madariaga (1994), Dynamic faulting under rate-dependent friction, *pure and applied geophysics*, *142*(3), 419–445, doi:10.1007/BF00876049.

Dempsey, D., and J. Suckale (2016), Collective properties of injection-induced earthquake sequences: 1. Model description and directivity bias, *Journal of Geophysical Research: Solid Earth*, *121*(5), 3609–3637, doi:10.1002/2015JB012550.

Dempsey, D., J. Suckale, and Y. Huang (2016), Collective properties of injection-induced earthquake sequences: 2. Spatiotemporal evolution and magnitude frequency distributions, *Journal of Geophysical Research: Solid Earth*, *121*(5), 3638–3665, doi:10.1002/2015JB012551.

Dieterich, J. H., and D. E. Smith (2009), Nonplanar Faults: Mechanics of Slip and Off-fault Damage, *Pure and Applied Geophysics*, *166*(10-11), 1799–1815, doi:10.1007/s00024-009-0517-y.

Dunham, E. M., D. Belanger, L. Cong, and J. E. Kozdon (2011a), Earthquake Ruptures with Strongly Rate-Weakening Friction and Off-Fault Plasticity, Part 1: Planar Faults, *Bulletin of the Seismological Society of America*, *101*(5), 2296–2307, doi:10.1785/0120100076.

Dunham, E. M., D. Belanger, L. Cong, and J. E. Kozdon (2011b), Earthquake ruptures with strongly rate-weakening friction and off-fault plasticity, part 2: Nonplanar faults, *Bulletin of the Seismological Society of America*, *101*(5), 2308–2322, doi:10.1785/0120100076.

Elsworth, W. C., and J. Suckale (2016), Rapid ice flow rearrangement induced by subglacial drainage in West Antarctica, *Geophysical Research Letters*, *43*(22), 697–11, doi:doi:10.1002/2016GL070430.

Fang, Z., and E. M. Dunham (2013), Additional shear resistance from fault roughness and stress levels on geometrically complex faults, *Journal of Geophysical Research: Solid Earth*, *118*(7), 3642–3654, doi:10.1002/jgrb.50262.

Freund, L. B. (1998), *Dynamic Fracture Mechanics*, Cambridge UP, Cambridge.

Gabriel, A.-A., J.-P. Ampuero, L. A. Dalguer, and P. M. Mai (2012), The transition of dynamic rupture styles in elastic media under velocity-weakening friction, *Journal of Geophysical Research: Solid Earth*, *117*(B9), doi:10.1029/2012JB009468.

Galis, M., J. P. Ampuero, P. M. Mai, and F. Cappa (2017), Induced seismicity provides insight into why earthquake ruptures stop, *Science Advances*, *3*(12).

Häring, M. O., U. Schanz, F. Ladner, and B. C. Dyer (2008), {C}haracterisation of the {B}asel 1 enhanced geothermal system, *{G}eothermics*, *37*(5), 469–495, doi: http://dx.doi.org/10.1016/j.geothermics.2008.06.002.

Kozdon, J. E., E. M. Dunham, and J. Nordström (2012), Interaction of waves with frictional interfaces using summation-by-parts difference operators: Weak enforcement of nonlinear boundary conditions, *Journal of Scientific Computing*, *50*(2), 341–367, doi: 10.1007/s10915-011-9485-3.

Kozdon, J. E., E. M. Dunham, and J. Nordström (2013), Simulation of dynamic earthquake ruptures in complex geometries using high-order finite difference methods, *Journal of Scientific Computing*, *55*(1), 92–124, doi:10.1007/s10915-012-9624-5.

Maurer, J. (2020), 2D Rough Fault Simulations of Induced Earthquakes, doi: https://doi.org/10.17605/OSF.IO/TMWCF.

Maurer, J., and P. Segall (2018), Magnitudes of Induced Earthquakes in LowâĂŘStress Environments, *Bulletin of the Seismological Society of America*, doi: 10.1785/0120170295.

McGarr, A. (2014), Maximum magnitude earthquakes induced by fluid injection, *Journal of Geophysical Research: Solid Earth*, *119*(2), 1008–1019, doi:10.1002/2013JB010597.

McGarr, A., and A. J. Barbour (2017), Wastewater Disposal and the Earthquake Sequences During 2016 Near Fairview, Pawnee, and Cushing, Oklahoma, *Geophysical Research Letters*, *44*(18), 9330–9336, doi:10.1002/2017GL075258.

Noda, H., E. M. Dunham, and J. R. Rice (2009), Earthquake ruptures with thermal weakening and the operation of major faults at low overall stress levels, *Journal of Geophysical Research*, *114*(B7), B07,302, doi:10.1029/2008JB006143.

Norbeck, J. H., and R. N. Horne (2018), Maximum magnitude of injection-induced earthquakes: A criterion to assess the influence of pressure migration along faults, *Tectonophysics*, *733*, 108–118, doi:https://doi.org/10.1016/j.tecto.2018.01.028.

Rice, J. R. (1983), Constitutive relations for fault slip and earthquake instabilities, *Pure and Applied Geophysics PAGEOPH*, *121*(3), 443–475, doi:10.1007/BF02590151.

Rudnicki, J. W. (1986), Fluid mass sources and point forces in linear elastic diffusive solids, *Mechanics of Materials*, *5*(4), 383–393, doi:http://dx.doi.org/10.1016/0167-6636(86)90042-6.

Sagy, A., and E. E. Brodsky (2009), Geometric and rheological asperities in an exposed fault zone, *Journal of Geophysical Research: Solid Earth*, *114*(B2), doi:10.1029/2008JB005701.

Shapiro, S. a., O. S. Krüger, C. Dinske, and C. Langenbruch (2011), Magnitudes of induced earthquakes and geometric scales of fluid-stimulated rock volumes, *GEOPHYSICS*, *76*(6), WC55–WC63, doi:10.1190/geo2010-0349.1.

Shapiro, S. A., O. S. Krüger, and C. Dinske (2013), Probability of inducing given-magnitude earthquakes by perturbing finite volumes of rocks, *Journal of Geophysical Research: Solid Earth*, *118*(7), 3557–3575, doi:10.1002/jgrb.50264.

van der Elst, N. J., M. T. Page, D. A. Weiser, T. H. Goebel, and S. M. Hosseini (2016), Induced earthquake magnitudes are as large as (statistically) expected, *Journal of Geophysical Research: Solid Earth*, *121*(6), 4575–4590, doi:10.1002/2016JB012818.

Walsh, F. R. I., and M. D. Zoback (2016), Probabilistic assessment of potential fault slip related to injection-induced earthquakes: Application to north-central Oklahoma, USA, *Geology*, *44*(12), 991–994, doi:10.1130/G38275.1.

Zheng, G., and J. R. Rice (1998), Conditions under which velocity-weakening friction allows a self-healing versus a cracklike mode of rupture, *Bulletin of the Seismological Society of America*, *88*(6), 1466–1483.

Figure 1.

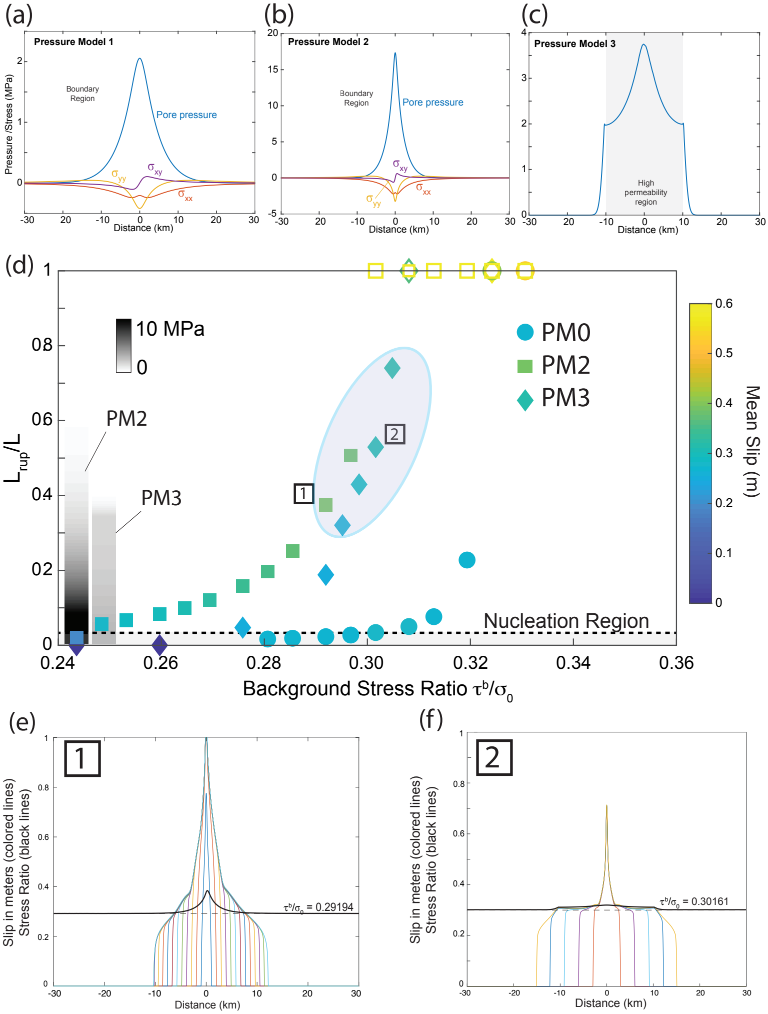

(a)
Pressure Model 1
Boundary Region
Pore pressure
Pressure /Stress (MPa)
Distance (km)
(b)
Pressure Model 2
Boundary Region
Pore pressure
Distance (km)
(c)
Pressure Model 3
High permeability region
Distance (km)
(d)
10 MPa
0
PM2
PM3
PM0
PM2
PM3
1
2
Nucleation Region
Background Stress Ratio τ^b/σ_0
L_{rup}/L
Mean Slip (m)
(e)
1
Slip in meters (colored lines)
Stress Ratio (black lines)
τ^b/σ_0 = 0.29194
Distance (km)
(f)
2
Slip in meters (colored lines)
Stress Ratio (black lines)
τ^b/σ_0 = 0.30161
Distance (km)

Figure 2.

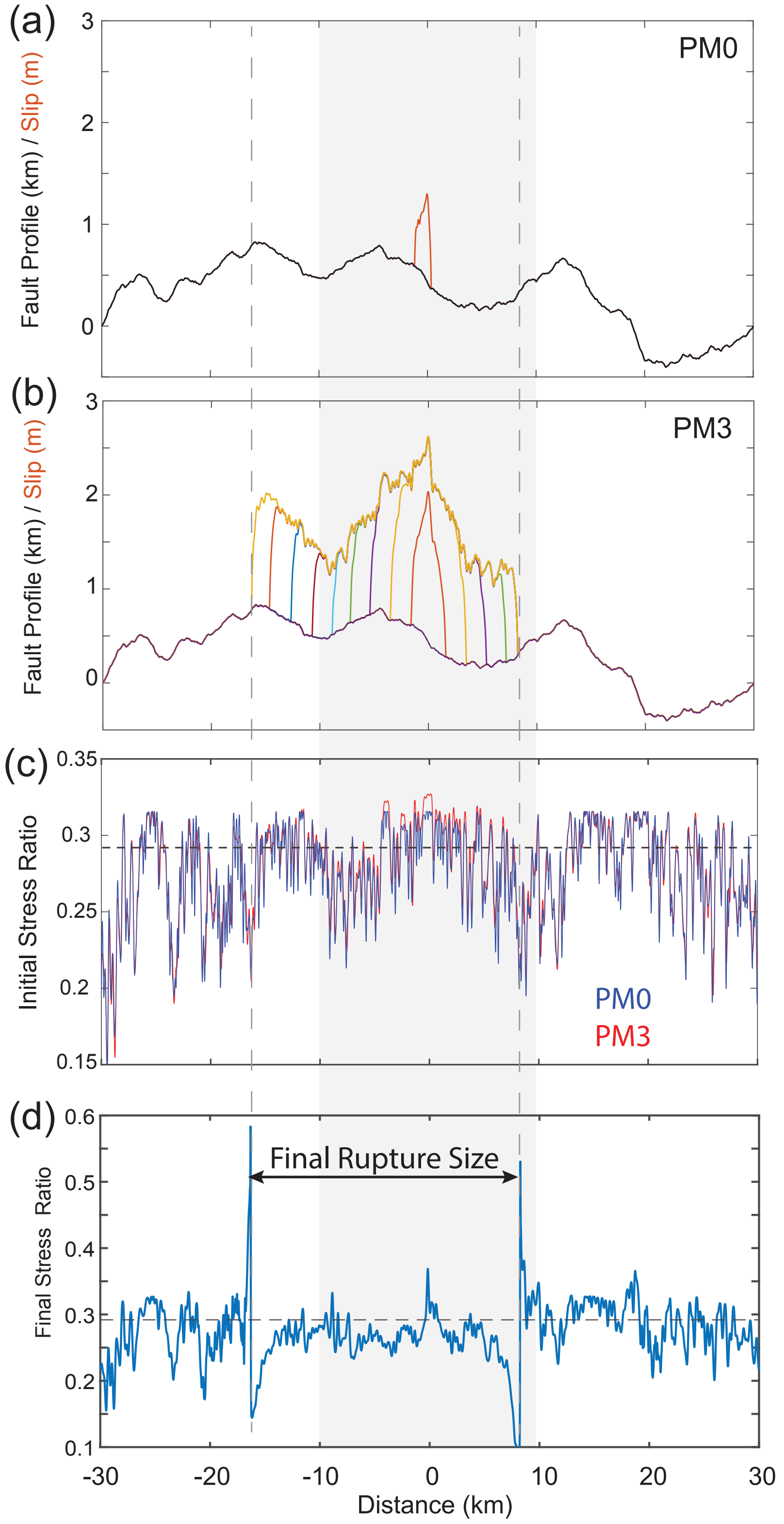

(a)
PM0
Fault Profile (km) / Slip (m)
(b)
PM3
Fault Profile (km) / Slip (m)
(c)
Initial Stress Ratio
PM0
PM3
(d)
Final Stress Ratio
Final Rupture Size
Distance (km)

Figure 3.

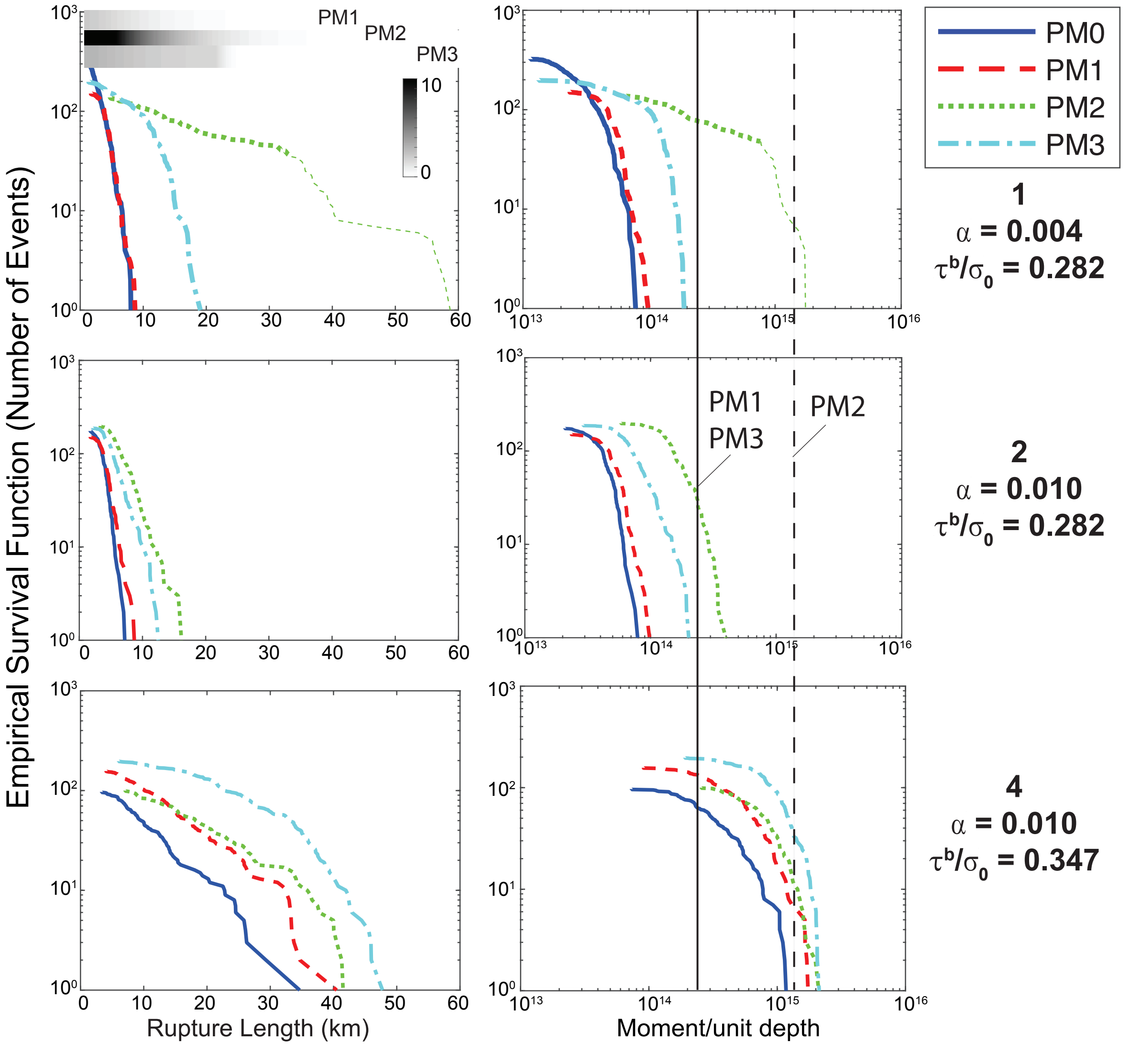

PM0
PM1
PM2
PM3
1
α = 0.004
τ^b/σ_0 = 0.282
2
α = 0.010
τ^b/σ_0 = 0.282
4
α = 0.010
τ^b/σ_0 = 0.347
PM1
PM3
PM2
10
0
Empirical Survival Function (Number of Events)
Rupture Length (km)
Moment/unit depth

Figure 4.

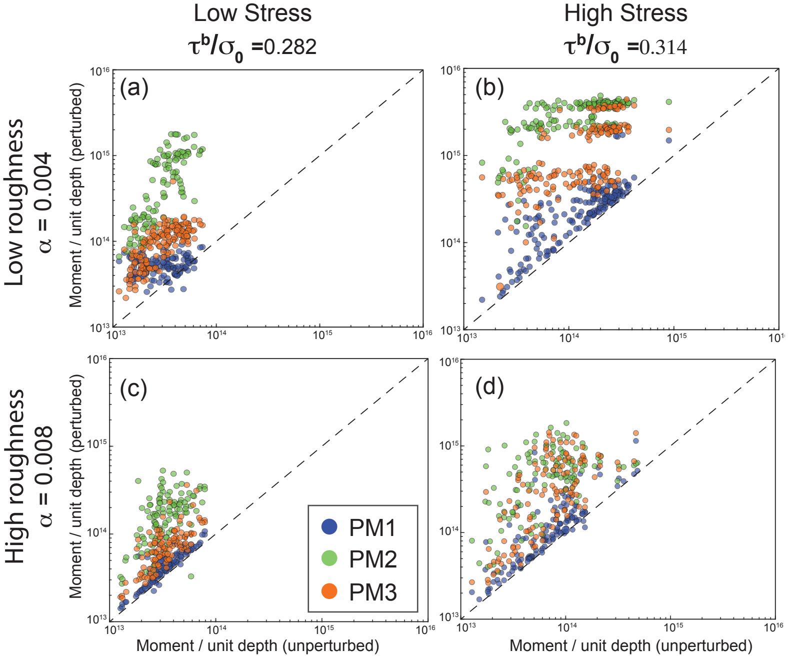

Low Stress
τ^b/σ_0 =0.282
High Stress
τ^b/σ_0 =0.314
Low roughness
α = 0.004
High roughness
α = 0.008
(a)
(b)
(c)
(d)
Moment / unit depth (perturbed)
Moment / unit depth (unperturbed)
PM1
PM2
PM3

Supporting Information for "Role of fluid injection on earthquake size in dynamic rupture simulations on rough faults"

Jeremy Maurer,[1,2] Paul Segall,[1] and Eric M. Dunham[1]

Contents of this file

Corresponding author: Jeremy Maurer, Missouri University of Science and Technology (jmaurer@mst.edu)

[1]Department of Geophysics, Stanford University, Stanford, California, USA

[2]Now in the Geological Engineering program, Missouri University of Science and Technology, Rolla, MO, USA.

Text S1: Details of the rupture simulator

Supp. Fig. S1 shows the problem geometry. Full details of the model are given in the papers cited in the main text; here we summarize the governing equations and initial conditions for our simulations. The medium is idealized as a Drucker-Prager elastic-plastic solid, which permits off-fault plastic relaxation of stress at high strains [see *Dunham et al.*, 2011]. Off-fault plasticity is important in the context of rough faults because plastic (i.e., irreversible) strain bounds stresses that with pure elasticity would grow extremely large due to slip on the rough fault.

We use a strong rate-weakening (SRW) friction law in our simulations. Friction obeys ordinary rate-and-state (ORS) friction at low velocities, and transitions to a very weak dynamic friction value (μ_w) above a critical weakening velocity V_W. Steady-state friction is given by:

$$\mu_{ss}(V) = \mu_w + \frac{\mu^{LV} - \mu_w}{[1 + (V/V_W)^n]^{(1/n)}} \tag{1}$$

where V is fault slip rate, the exponent n governs how rapidly the transition from ordinary to weak friction occurs, and μ^{LV} is the conventional low-velocity friction coefficient:

$$\mu^{LV} = \mu_0 - (b - a) \ln (V/V_0).$$

with parameters $\mu_0 = \mu_{ss}(V_0)$, a, b, and V_0 =reference velocity. We use a regularized rate-and-state friction law in the slip law form [*Rice*, 1983; *Noda et al.*, 2009]:

$$\mu^{LV}(V, \Theta) = a \,\mathrm{arcsinh} \left(\frac{V}{2V_0} e^{\Theta/a} \right) \tag{2}$$

with state Θ (note the difference between Θ used here and θ used in many theoretical papers on ORS friction, they are related by $\Theta = \mu_0 + b \ln(\theta/\theta_0)$). In general we adopt the same parameter values as *Dunham et al.* [2011], who use a fully weakened friction coefficient of $\mu_w = 0.13$ and weakening velocity $V_W = 0.17$ m/s (see Tables in the Supplemental Material for all parameter values).

FDMAP uses the slip law for state evolution:

$$\frac{d\Theta}{dt} = -\frac{V}{d_c}\left(\mu(V,\Theta) - \mu_{ss}(V)\right) \tag{3}$$

The initial state Θ_{ini} is specified as a constant over the entire fault and the initial velocity on the fault is chosen to be consistent with this value and the locally-resolved stress on the fault. Because stress is heterogeneous for rough faults, the initial velocity is also heterogeneous and for very rough faults can vary over 10 orders of magnitude. Initial velocity in our SRW simulations is always below $V_0 = 10^{-6}$ m/s.

An important parameter in SRW-friction simulations under low stress conditions is τ^{pulse}, defined as the largest shear stress τ_0^b such that

$$\tau_0^b - \frac{G}{2c_s}V \leq \sigma_0\mu_{ss}(V)$$

for all $V > 0$, where c_s is the shear wave speed [*Zheng and Rice*, 1998]. For rough faults, this expression is modified to include an additional term due to roughness drag (see below). Dynamic earthquake simulations using a SRW friction law lead to pulse-like ruptures when the background stress is close to τ^{pulse}. Rupture style transitions to crack-like at sufficiently high stress levels. Pulse-like ruptures on rough faults may self-arrest naturally due to fluctuations in the local stress around fault bends, or if the background stress is high enough they may rupture the entire fault. Because dynamic friction is very weak, the background stress required to sustain ruptures (approximately τ^{pulse}) can be much lower than the static frictional strength of the fault.

For initial stresses that are a significant fraction of the static strength, (how large depends on roughness), ruptures grow indefinitely. *Fang and Dunham* [2013] considered background shear/normal stress ratios of 0.28-0.4, much lower than values typically associated with static friction (0.6-0.8). To nucleate an event, stress must still reach static strength (0.7 in our simulations), but once nucleated events can propagate at much lower stress levels. For more details about the model, see references in the main text.

The faults in our simulations are 60 km, which is longer than most induced earthquakes; however, length scales can be normalized using the length of the state evolution region at the rupture tip (R_0) [*Dunham et al.*, 2011, and references therein]:

$$R_0 \approx \frac{3\pi}{4}\frac{Gd_c}{\tau^p - \tau^r} \tag{4}$$

for shear modulus G, critical state evolution distance d_c. Peak stress τ^p can be estimated as

$$\tau^p \approx \sigma_0 \left[a \log\left(V^p/V_0\right) + \Theta_{\text{ini}}\right] \tag{5}$$

and residual stress τ^r is

$$\tau^r \approx \sigma_0 \mu_{ss}\left(V^{\text{pulse}}\right) \tag{6}$$

V^p is the peak velocity at dynamic speeds, approximately 1 m/sec, V^{pulse} is the steady-state velocity at τ^{pulse}, and Θ_{ini} is the initial state on the fault (see Eq. 2 and discussion). For the simulations discussed in this section, $\tau^p - \tau^r \approx 60$ MPa and $d_c \approx 0.05$ m, so R_0 is of order 100 m.

Fault profiles are constructed by filtering zero-mean white noise to have the desired spectral properties and shifting the profile so that the endpoints are located at $y = 0$ and the highest resolved shear/normal stress ratio at wavelengths larger than the approximate nucleation dimension is at the origin. For our study, this dimension is approximated by L_b:

$$L_b = \frac{G^* d_c}{b\sigma_0} \tag{7}$$

and is about 1.6 km.

Text S2: Diffusion in a medium with a permeable channel

To introduce a finite length scale into the pore pressure diffusion problem, we introduce a high-permeability channel that crosses the domain and the fault (Supp. Fig. S2). The injector is located inside this channel, and pressure diffuses through the channel to the fault. The domain as total length $2L = 60$ km, and total width $L = 30$ km. The length of the channel is $2L_k$.

The governing equations are:

$$\nabla \cdot [D(x)\nabla p] = \frac{\partial p}{\partial t} + \frac{q}{\rho_f \phi \beta}\delta(x)\delta(y - y_0)H(t) \tag{8}$$

for diffusivity $D(x) = \kappa(x)/(\phi\eta\beta)$, where κ is permeability, η is fluid viscosity, ϕ is porosity, and β is the fluid compressibility. x_0 is the location of the fluid injector. $\kappa(x) = \kappa_1$ if $|x| > L_k$, and $\kappa(x) = \kappa_2$ if $|x| < L_k$; also with D_1 and D_2. q is the (constant) fluid mass flux, ρ_f is the fluid density, δ is the Dirac delta function, and $H(t)$ is the Heaviside unit step function. We assume all properties are constants except permeability takes a high value inside the channel (κ_2), and a low value outside (κ_1).

To solve this system, we discretize the domain into a uniform grid and solve using an algorithm developed by *Elsworth and Suckale* [2016]. Supp. Table S5 gives the parameter values we use for solving for pore pressure in the channel. We assume zero-pressure boundary conditions at the top and bottom of the domain, and zero-gradient conditions at the left and right sides of the domain, and neglect poroelastic effects in this analysis. Supp. Fig. S3 shows the pressure distribution after 100 days and 1000 days.

S3: Impact of limited roughness resolution on rupture size

In the simulator we use, artificially-nucleated earthquakes can propagate at stress levels less than 0.6-0.7, at which most faults in the crust, particularly in intra-cratonic settings, are thought to operate [e.g., *Walsh and Zoback*, 2015] . The reason for this is that on "smooth" faults, i.e. where roughness down to the wavelength of slip is not modeled, strong rate-weakening friction allows rupture propagation at much lower stress levels than static failure.

Fang and Dunham [2013] address this issue in their study, and point out that many laboratory experiments show that fault materials undergo significant weakening at high slip speeds. They postulate that the additional resistance to slip related to the propagation of the rupture around bends in the fault, termed "roughness drag" (τ^{drag}), is responsible for the difference between the low friction measured in the lab and the shear/normal stress ratios implied by more traditional fault studies. They derived an approximate expression for τ^{drag}, given in Eq. 2 in the main text, which depends on fault roughness α as well as the minimum roughness wavelength λ_{min}. Their derivation is based on the scaling pointed out by *Dieterich and Smith* [2009]:

$$\tau^{\text{drag}} \propto \frac{\alpha^2 \Delta}{\lambda_{\text{min}}}$$

where Δ is slip. In our simulations, $\Delta/\lambda_{\text{min}} \approx 0.01$, so τ^{drag} ranges from 0.1-10 MPa for $\alpha = 0.001 - 0.01$. However, for lower values of the minimum roughness wavelength τ^{drag} can increase substantially. As *Fang and Dunham* [2013] point out, as the minimum wavelength approaches the scale of slip, pervasive off-fault yielding is expected to occur, leading to shear over normal stress ratios approximately equal to the internal friction coefficient of the host rock, which may be 0.6-0.8.

Fang and Dunham [2013] estimate that, accounting for roughness down to the scale of slip, the resistance drag stress during slip due to roughness τ^{drag} is on the order of 10 MPa for $\alpha = 0.001$ and could approach the background level for high roughness. As they point out, this could explain the discrepancy between low values of friction observed in laboratory experiments of dynamic friction and classic estimates. Supp. Fig. S12 shows how rupture size changes as the minimum roughness wavelength changes.

In the majority of the simulations shown in this study, the minimum roughness wavelength is 300 m. With this value, $\Delta/\lambda_{\text{min}} \approx 10^{-3}$, so τ^{drag} in our simulations is about a factor of 1000 smaller than expected if roughness on crustal faults scales down to the scale of slip. We conducted a limited number of simulations using roughness wavelengths of 150 and 600 meters to compare to the reference case. Figure S12 shows how the resistance to slip due to roughness drag scales with λ_{min}, roughness α, and slip Δ. S12a shows, for the limited range of λ_{min} we test in our simulations, how the median rupture length (out of 100 simulations) changes for a given stress level and two different roughnesses. S12b shows the theoretical scaling of τ^{drag} with λ_{min}, the vertical lines represent the three values used in plot (a). It is clear that having the computational ability to allow roughness wavelengths down to the meter level would significantly increase the background stress necessary to sustain dynamic rupture.

We also show scatter plots of τ^{drag} versus rupture length in Figure S13. These plots clearly demonstrate the change in rupture size that occurs as the minimum roughness wavelength changes. Note that for these simulations, the fault is the same at wavelengths greater than 600 meters. The additional roughness due to refining λ_{min} does not necessarily contribute to higher stresses, but to stress variations on smaller scales. These variations lead to more plastic yielding from larger strains and also may contribute to increased radiation, both of which dissipate energy from the propagating rupture, and so the overall rupture length tends to end up smaller.

References

Dieterich, J. H., and D. E. Smith (2009), Nonplanar Faults: Mechanics of Slip and Off-fault Damage, *Pure and Applied Geophysics*, *166*(10-11), 1799–1815, doi: 10.1007/s00024-009-0517-y.

Dunham, E. M., D. Belanger, L. Cong, and J. E. Kozdon (2011), Earthquake Ruptures with Strongly Rate-Weakening Friction and Off-Fault Plasticity, Part 1: Planar Faults, *Bulletin of the Seismological Society of America*, *101*(5), 2296–2307, doi: 10.1785/0120100076.

Elsworth, W. C., and J. Suckale (2016), Rapid ice flow rearrangement induced by subglacial drainage in West Antarctica, *Geophysical Research Letters*, *43*(22), 697–11, doi: doi:10.1002/2016GL070430.

Fang, Z., and E. M. Dunham (2013), Additional shear resistance from fault roughness and stress levels on geometrically complex faults, *Journal of Geophysical Research: Solid Earth*, *118*(7), 3642–3654, doi:10.1002/jgrb.50262.

Noda, H., E. M. Dunham, and J. R. Rice (2009), Earthquake ruptures with thermal weakening and the operation of major faults at low overall stress levels, *Journal of Geophysical Research*, *114*(B7), B07,302, doi:10.1029/2008JB006143.

Rice, J. R. (1983), Constitutive relations for fault slip and earthquake instabilities, *Pure and Applied Geophysics PAGEOPH*, *121*(3), 443–475, doi:10.1007/BF02590151.

Walsh, F. I. R., and M. D. Zoback (2015), Oklahoma's recent earthquakes and saltwater disposal, *Science Advances*, *1*(5), 1–9, doi:10.1126/sciadv.1500195.

Zheng, G., and J. R. Rice (1998), Conditions under which velocity-weakening friction allows a self-healing versus a cracklike mode of rupture, *Bulletin of the Seismological Society of America*, *88*(6), 1466–1483.

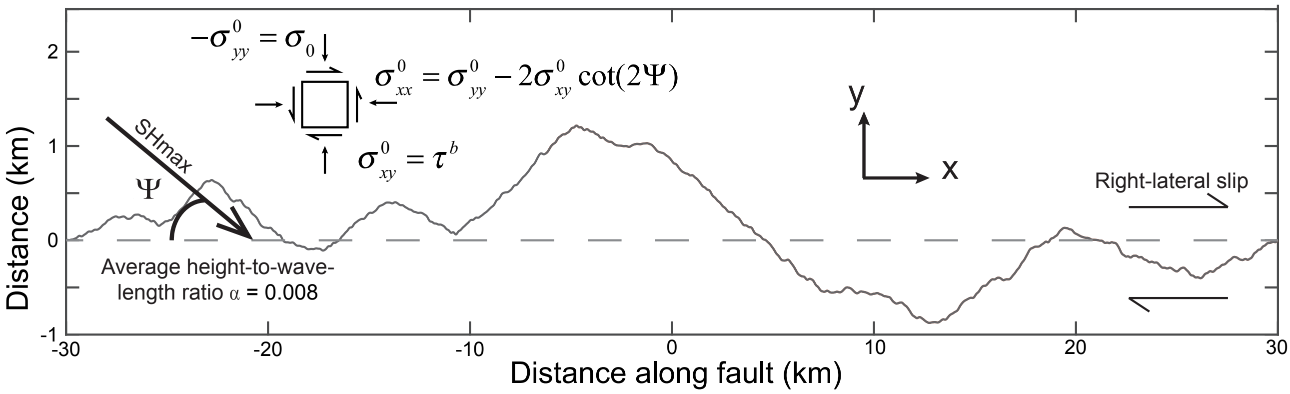

Figure S1. Diagram showing the basic geometry for the 1-D fault in 2-D medium, including the background stress tensor.

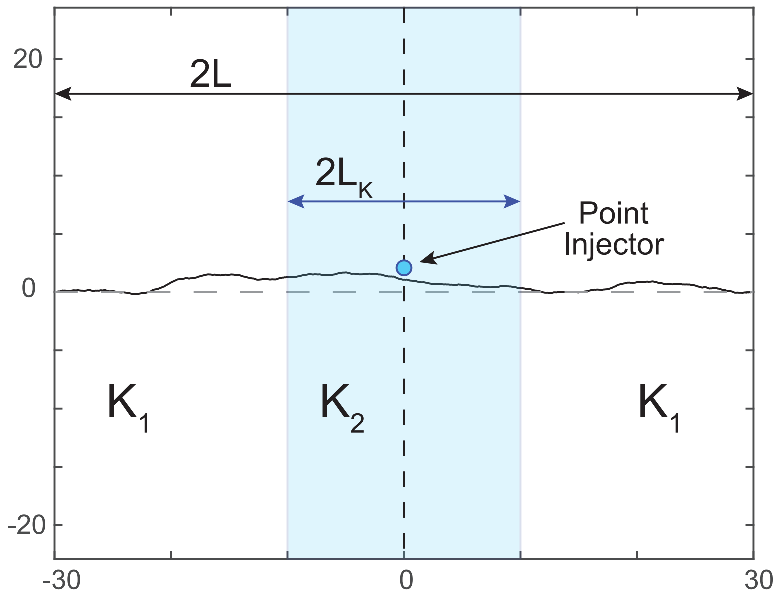

Figure S2. Geometry for the nonuniform permeability pressure model (PM3). Pressure is computed numerically after 1000 days on injection. The injector is located at $x = 0$, $y = 2$ km.

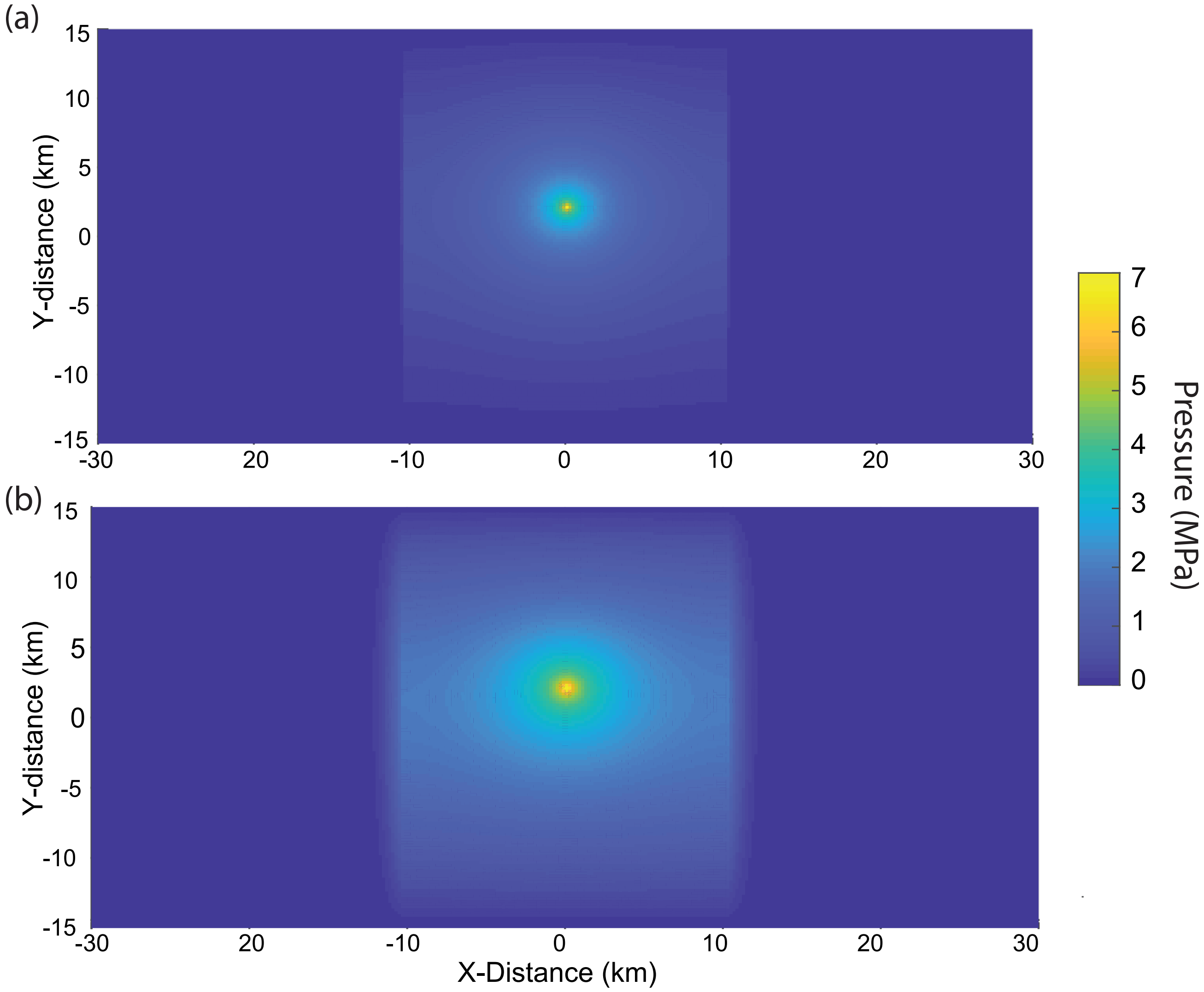

Figure S3. Pressure distribution after (a) 100 and (b) 1000 days of continuous, constant injection. Parameters are as given in Table S5. The horizontal dashed line is the nominal fault location at $y = 0$.

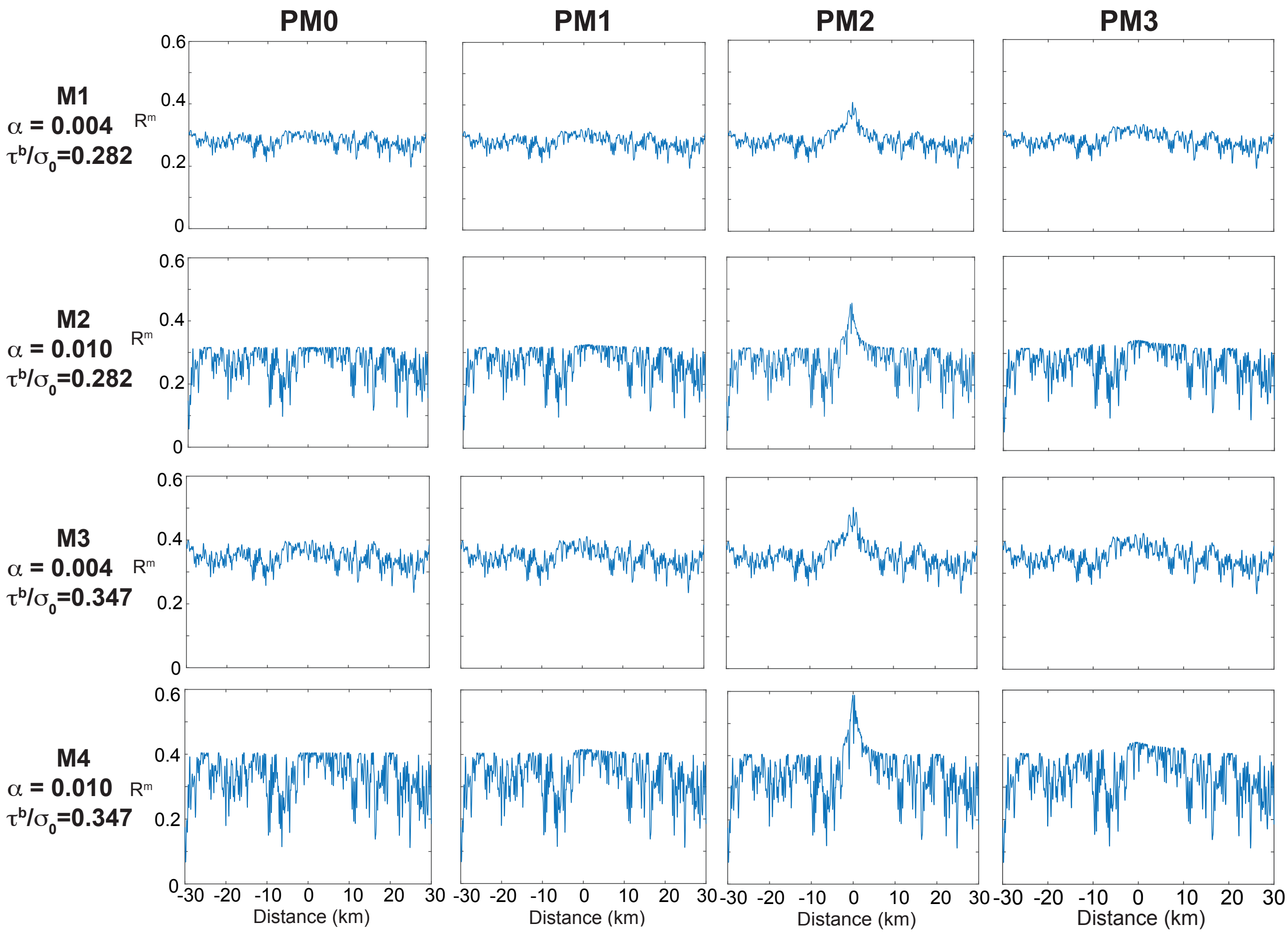

Figure S4. Initial Shear-to-normal stress ratio for each of the pressure models using four different combinations of background stress ratio and roughness. For comparison, static friction is 0.7.

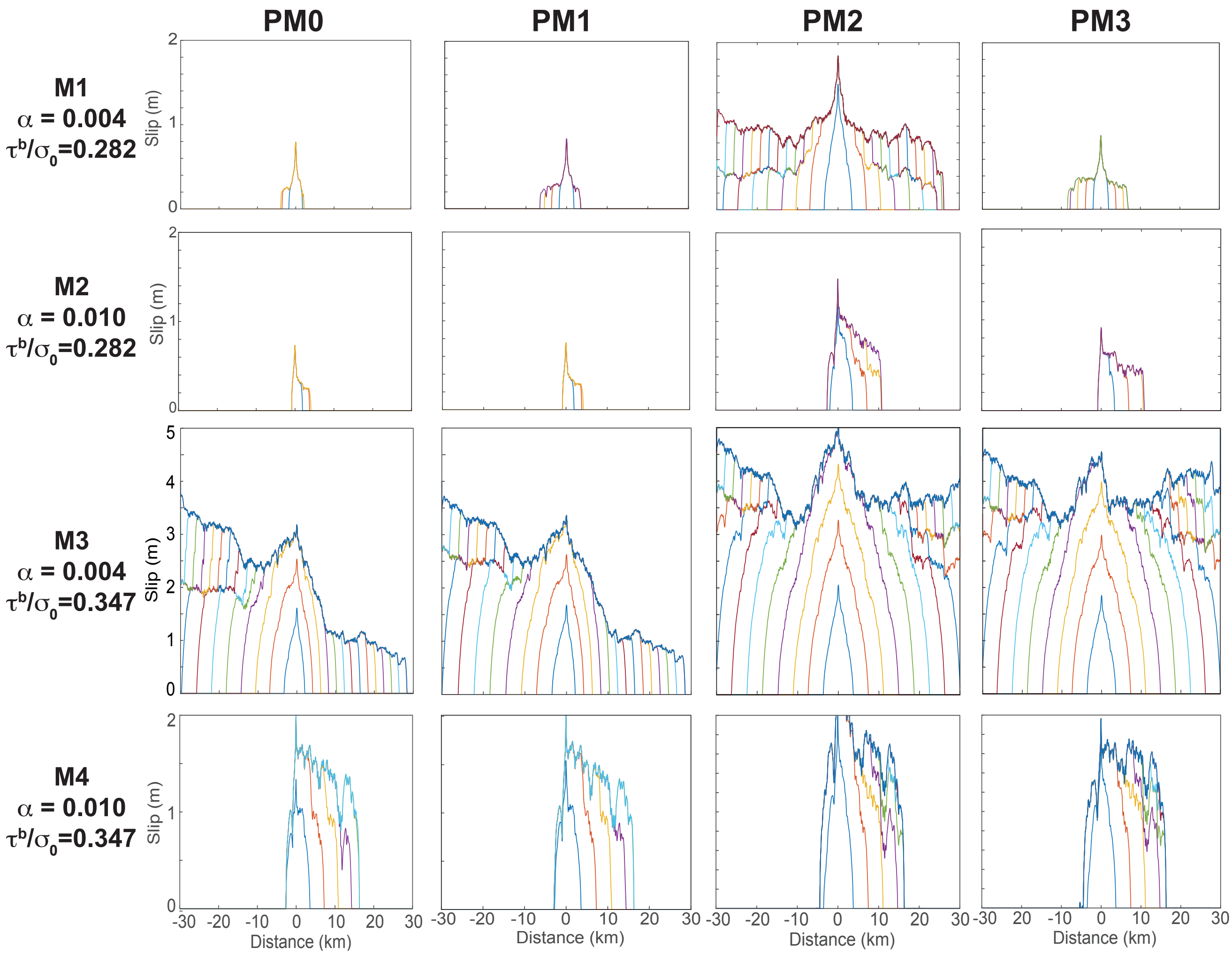

Figure S5. Slip during dynamic rupture for each of the models shown in Supp. Fig. S5. Slip is shown at regular time intervals of 0.7 seconds. Colors are for visual aid only. Note that the vertical scale for M3 ruptures is 5 m, compared to 2 m for the others.

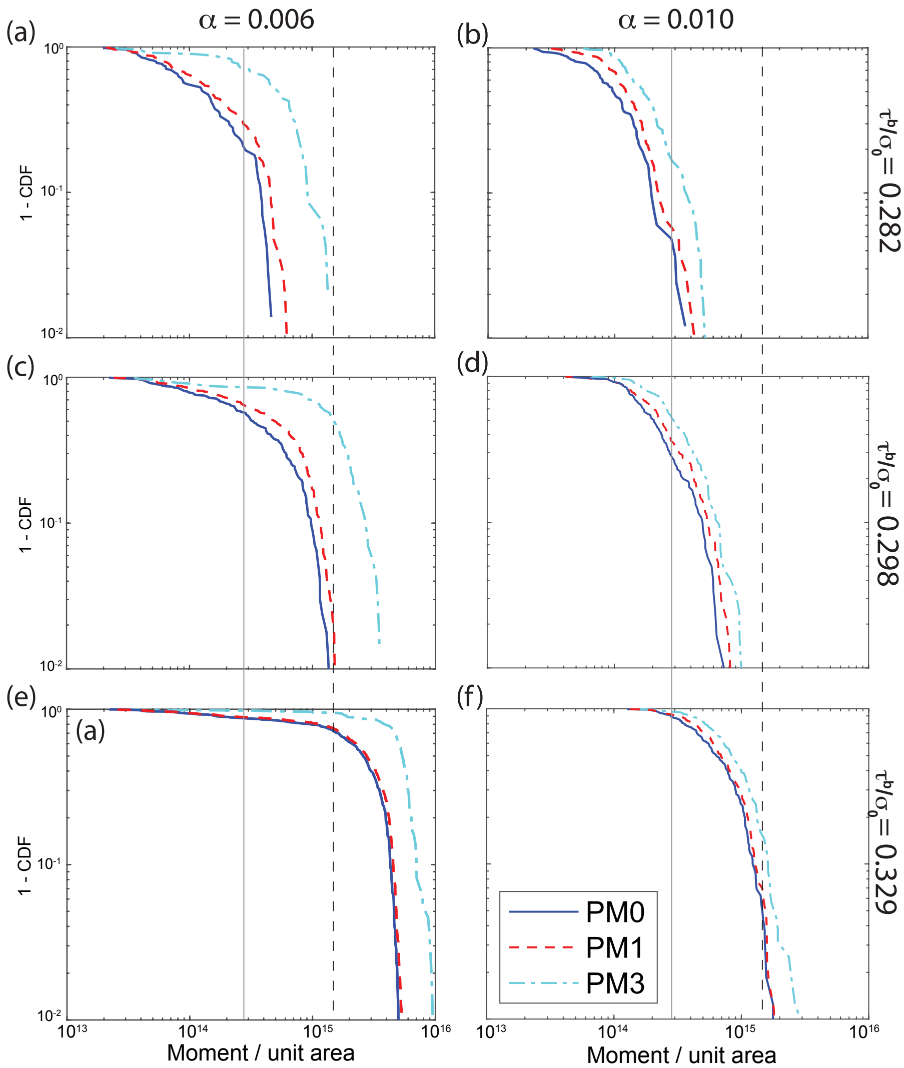

Figure S6. Frequency-moment distributions for PM0, PM1, and PM3 using a background normal stress equal to 126 MPa. PM2 simulations were not conducted for this normal stress value (126 MPa) because $\sim$ 20 MPa peak pressure perturbation was not thought to be likely at the corresponding depths. Vertical lines show Mmax consistent with Figure 3 in the main text.

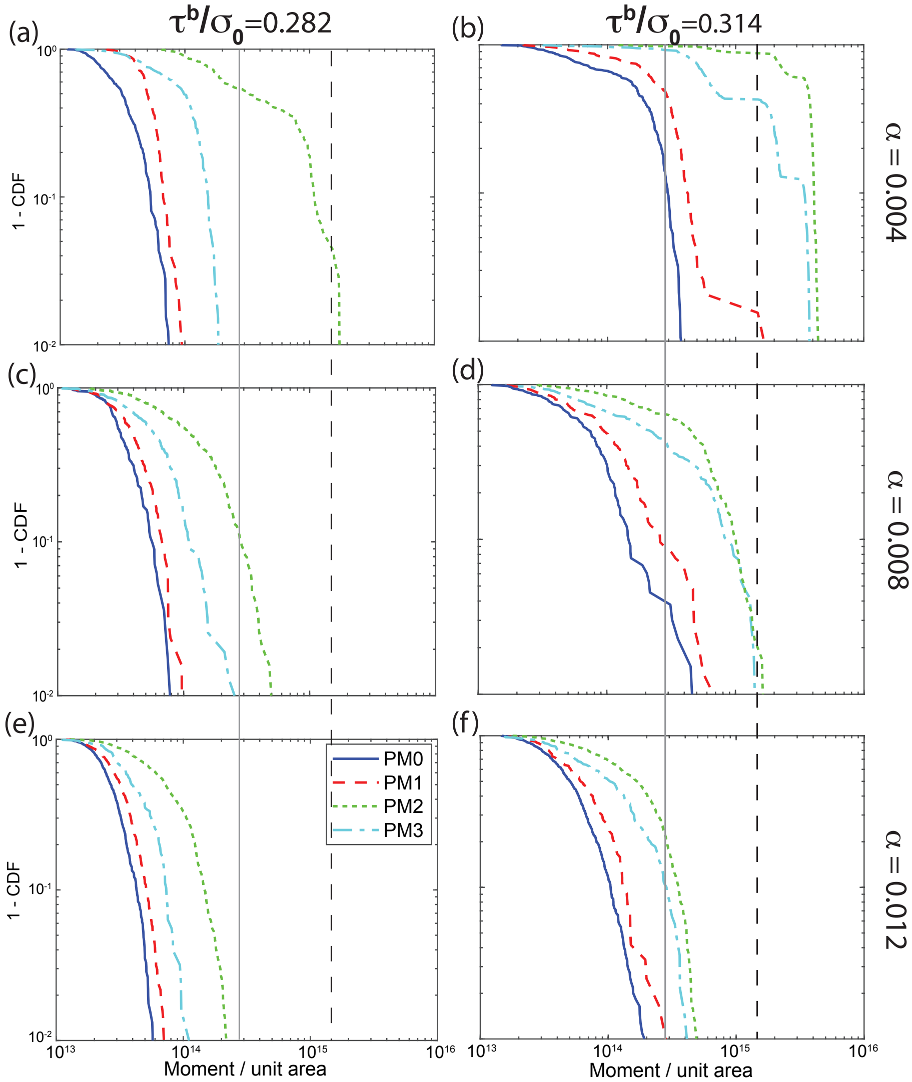

Figure S7. Additional frequency-moment distributions for each of the pressure models using $\sigma_0 = 62$ MPa. (a) is the same as shown in Figure 3 in the main text, but the distributions are normalized to the inverse CDF.

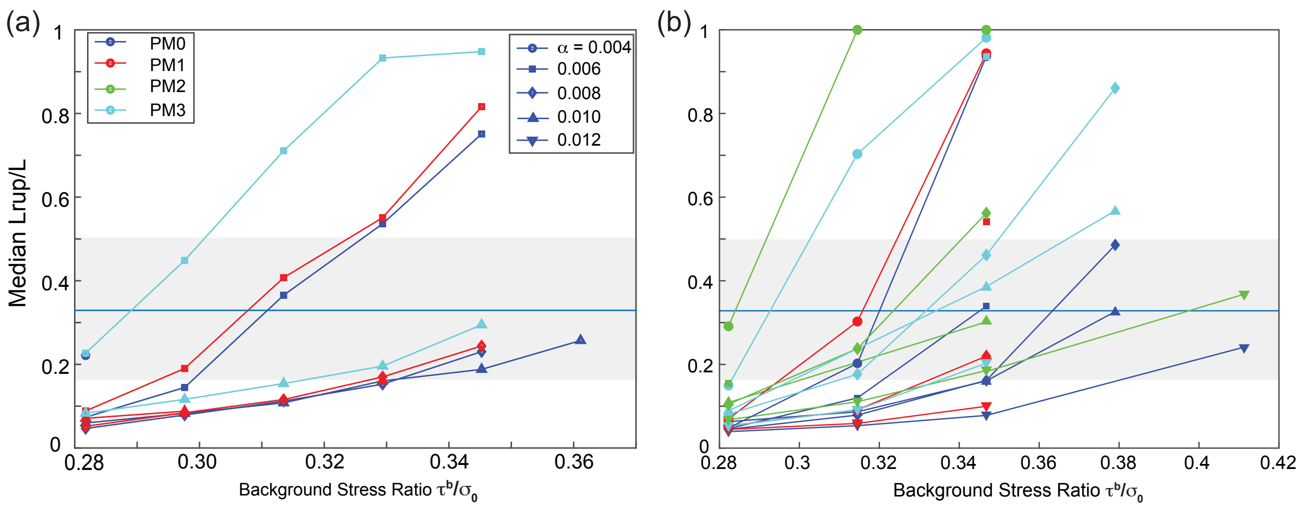

Figure S8. Median normalized rupture length as a function of background stress for (a) high background normal stress (126 MPa) and (b) low background normal stress (62 MPa). Colors represent pressure models and symbol types are roughnesses. The shaded region and solid blue line are the same as in Fig. 1 in the main text, and represent the pressure boundary region for the diffusive models (PM1, PM2) and the width of the high-permeability region for PM3. Each point on the plot represents the median out of 200 simulations.

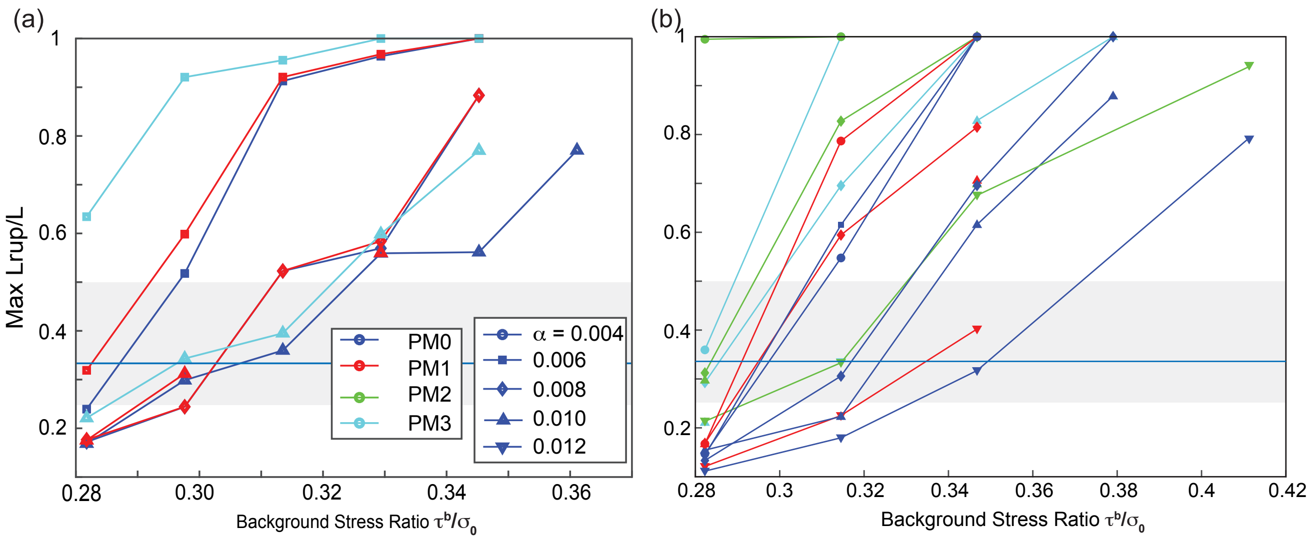

Figure S9. Same as Fig. S8, but for maximum normalized rupture length. (a) High background normal stress. (b) Low background normal stress.

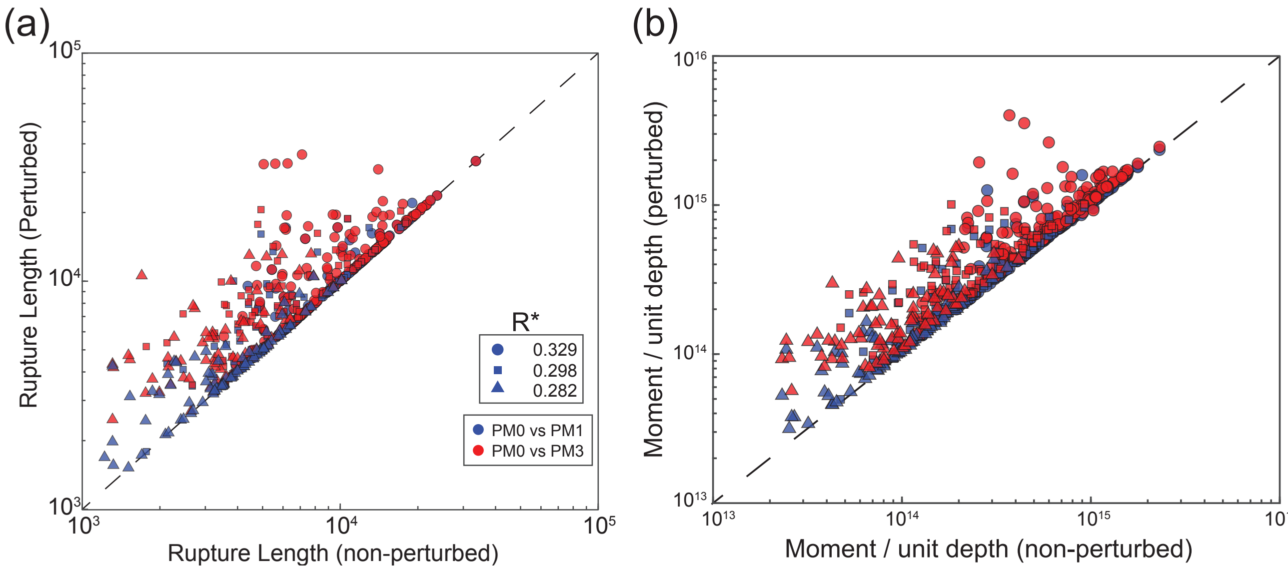

Figure S10. Scatter plots comparing perturbed and non-perturbed event sizes for $\alpha = 0.010$ and $\sigma_0 = 126$ MPa, for (a) rupture length (meters) (b) moment per unit depth (N m /m). Symbol type denotes the background stress level. Blue symbols compare PM0 and PM1, red compare PM0 with PM3. Maximum rupture length is 60 km (6×10^4 m) with corresponding moment approximately 5×10^{15} N m/m.

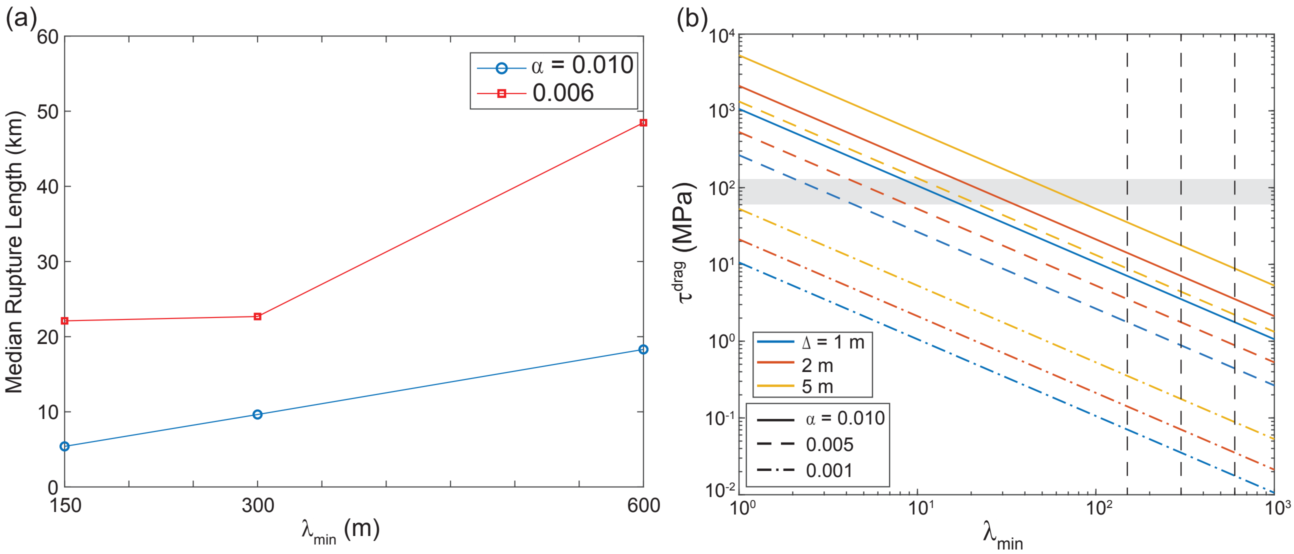

Figure S12. (a) Median rupture length in km out of 100 simulations, for three different values of λ_{min} and two roughnesses. A simple linear fit gives a slope of approximately 0.03 for $\alpha = 0.010$ and 0.09 for $\alpha = 0.006$. (b) Theoretical scaling of τ^{drag} with λ_{min} for various values of slip Δ and roughnesses. Vertical dashed lines are the values of λ_{min} used in (a). Note that these lines do not take into account the break in scaling resulting from pervasive off-fault damage, discussed in *Fang and Dunham* [2013]. The gray shaded region represents the range of stresses between the high- and low-normal stress cases presented in this study (62 and 126 MPa).

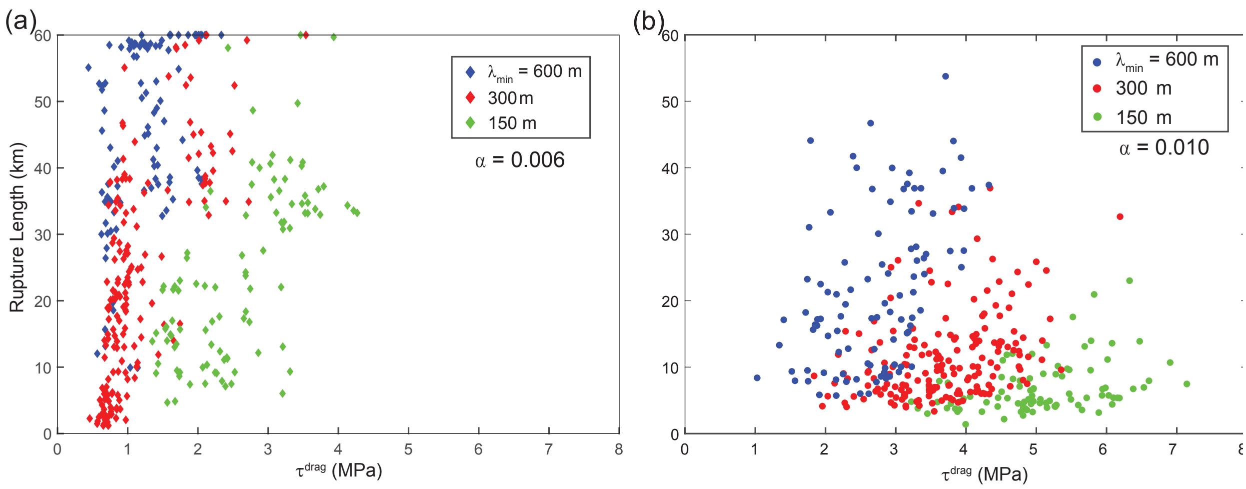

Figure S13. Scatter plots of rupture length versus τ^{drag} for (a) $\alpha = 0.006$, and (b) $\alpha = 0.010$, for three different values of λ_{min}.

Table S1. Frictional and stress parameters used in this study and in *Fang and Dunham* [2013]. These values are for the high normal stress calculations.

Parameter	Value
b	0.02
a	0.016
μ_0	0.7
d_c	0.0857 m
σ^0 (background normal stress)	126 MPa
τ^b (background shear stress)	variable (35.5 - 45.5 MPa)
G (shear modulus)	32.04 GPa
c_s (shear wave speed)	3.464 km/s
ν (Poisson's ratio)	0.25
$\Theta(t = 0)$ (initial state variable)	0.4367
μ (Related to the internal friction coefficient)	$\sin(\arctan(0.7)) = 0.5735$
Ψ (mean fault orientation)	50°

Table S2. Same as Table S1 but used for the low mean stress simulations with SRW. Values not repeated here are the same as in Table S1.

Parameter	Value
d_c	0.042 m
σ^0 (background normal stress)	62 MPa
τ^b (background shear stress)	variable (17.5-25.5 MPa)

Table S3. Parameters for Pressure Model 1.

Parameter	Value
ρ_f	1000 kg/m^3
c	0.36
α	0.4
λ	20 GPa
κ (permeability)	2.24×10^{-15} m^2
G (shear modulus)	32.04 GPa
η (viscosity)	$0.4 \times 10^{-3} Pa - s$
ν (Poisson's ratio)	0.25
q (mass flux)	0.05 m^3/s
B	0.5
λ_u	30 GPa
10-kPa width	19 km
Origin	[0, 2 km]

Table S4. Parameters for Pressure Model 2. Those not given are identical to PM1.

Parameter	Value
c	0.1
q (mass flux)	0.28 m^3/s
10-kPa half-width	12.5 km
Stretch	Y-direction, 4x

Table S5. Parameter values used for the three-zone pressure diffusion problem.

Parameter	Value
κ_1	10^{-16} m^2
κ_2	10^{-13} m^2
ρ_f (Fluid density)	1000 kg/m^3
p_0 (Initial pressure)	0 MPa
η (Fluid viscosity)	4×10^{-4} Pa s
β (Fluid compressibility)	3.2×10^{-10} 1/Pa
ϕ (porosity)	0.12
q (Mass injection rate)	2 kg/sec
L	30 km
L_k	10 km
y_0 (Injector Location)	2 km
h	200 m
Δt	1000 sec
$D_1 = \kappa_1/(\phi\beta\eta)$	0.0065 m^2/s
$D_2 = \kappa_2/(\phi\beta\eta)$	6.5 m^2/s